INL/JOU-25-86993-Revision-0

Characterization of in-situ and ex-situ Ion-Irradiated Additively Manufactured 316L and 316H Stainless Steels

August 2025

Wei-Ying Chen, Stephen Taller, Andrea M. Jokisaari, Yiren Chen, Rongjie Song, Lin Gao, Peter M. Baldo, Dzmitry Habaruk, Meimei Li

Changing the World's Energy Future

Idaho National Laboratory

INL is a U.S. Department of Energy National Laboratory operated by Battelle Energy Alliance, LLC

INL/JOU-25-86993-Revision-0

Characterization of in-situ and ex-situ Ion-Irradiated Additively Manufactured 316L and 316H Stainless Steels

Wei-Ying Chen, Stephen Taller, Andrea M. Jokisaari, Yiren Chen, Rongjie Song, Lin Gao, Peter M. Baldo, Dzmitry Habaruk, Meimei Li

August 2025

Idaho National Laboratory
Idaho Falls, Idaho 83415

http://www.inl.gov

Prepared for the
U.S. Department of Energy
Under DOE Idaho Operations Office
Contract DE-AC07-05ID14517

Characterization of *in-situ* and *ex-situ* Ion-Irradiated Additively Manufactured 316L and 316H Stainless Steels*

Wei-Ying Chen[1], Stephen Taller[2], Andrea M. Jokisaari[3], Yiren Chen[1], Rongjie Song[3], Xuan Zhang[1], Lin Gao[1], Peter M. Baldo[1], Dzmitry Habaruk[1], and Meimei Li[1]

[1]**Argonne National Laboratory**

[2]**Oak Ridge National Laboratory**

[3]**Idaho National Laboratory**

ABSTRACT

Additively manufactured (AM) 316 stainless steel (SS) differs from its wrought counterpart in its unique dislocation cell structure and the presence of segregation and oxide particles at the cell walls. This work investigated the evolution of the microstructure in laser powder bed fusion (LPBF) 316L and 316H SS under *in-situ* 1 MeV Kr ion irradiation at 600℃ to 5 dpa, and *ex-situ* 4 MeV Ni ion irradiation at 300℃ and 600℃ from 0.2 dpa to 10 dpa, with a dose rate for all experiments of 10^{-3} dpa/s. The results reveal that the dislocation cell structure result in heterogeneous formation of dislocation loops and voids, particularly at 600℃, where loops tend to form within the cell interiors while voids form at the cell boundaries. LPBF 316H has a reduced level of swelling compared to LPBF 316L due to prolonged incubation. Energy Dispersive X-ray Spectroscopy (EDS) mapping indicates Ni and Si segregation at void surfaces due to radiation-induced segregation. At 300℃, where voids are absent, the distribution of dislocation loops and stacking fault tetrahedra appears to be uniform. Dislocation cell structures mostly disappeared by 2 dpa for all conditions in this work. $M_{23}C_6$ carbides were observed in LPBF 316H at 600℃ as early as 0.2 dpa, but not in LPBF 316L. Nanoindentation was performed to obtain the hardness of irradiated materials. This work illustrated the influence of additive manufacturing processes on microstructure evolution under irradiation, revealing the differences as well as the similarities as compared with wrought 316 SS, and the AM-related phenomenon that can potentially occur under neutron irradiation in nuclear reactors.

*This manuscript has been authored by UChicago Argonne LLC under Contract No. DE-AC02-06CH11357, by UT-Battelle, LLC, under contract DE-AC05-00OR22725, and Battelle Energy Alliance LLC under contract DE-AC07-05ID14517 with the U.S. Department of Energy.The US government retains and the publisher, by accepting the article for publication, acknowledges that the US government retains a nonexclusive, paid-up, irrevocable, worldwide license to publish or reproduce the published form of this manuscript, or allow others to do so, for US government purposes. DOE will provide public access to these results of federally sponsored research in accordance with the DOE Public Access Plan (https://www.energy.gov/doe-public-access-plan).

Keywords: Additive Manufacturing, Stainless Steel, Irradiation Effects, Dislocation Loops, Voids

1 INTRODUCTION

The emergence of metal additive manufacturing (AM) technologies have opened new avenues for advancing materials engineering. AM technologies allow for the rapid and cost-effective production of components with complex geometries, leading to a wide range of innovations in materials science and manufacturing. Consequently, AM materials have attracted significant attention in recent years as a novel approach to producing high-quality components with enhanced design and customization flexibility. While the compositions of AM materials can be similar to those of traditionally manufactured materials, they exhibit distinct microstructures. Microstructural characteristics arising from the printing process, such as porosity, anisotropic grain structures, inclusions, dislocation cells, and chemical inhomogeneity, are commonly observed. Before AM materials can be widely adopted, these microstructures, along with their behavior under operational conditions, must be evaluated.

Understanding how AM materials respond to irradiation in reactor environments is critical to ensuring the reliability and safety of nuclear reactor components [1, 2]. Like any new materials intended for use in reactors, AM materials must undergo careful assessment of their irradiation response. Among many AM materials, AM 316 stainless steels (SS) are of particular interest due to the heavy use of conventionally manufactured 316 SS as structural materials in light water reactors and as proposed core components in liquid metal-cooled fast reactors [3–11]. Certain microstructures unique to AM 316 are of special concern, as they may exhibit different behaviors under irradiation, deviating from their traditionally manufactured counterparts. A unique AM 316 microstructure is the dislocation cell structure observed in as-built AM stainless steels [5, 12]. Some studies suggested that the dislocation cell structure in AM 316 is beneficial to its mechanical properties [13, 14]. In addition, the high dislocation density offered by the dislocation cell structure may reduce irradiation swelling similar to that observed in the cold-worked (CW) stainless steels [3, 15–25]. However, recent ion irradiation studies indicate that AM 316 stainless steels actually swell more than their wrought or solution annealed counterparts when exposed to similar conditions [3, 7]. It is important to gather more data to confirm this observation and to determine the controlling physical mechanisms. Especially, previous studies only investigated the high-dose (several tens to hundreds of dpa) microstructure of irradiated AM 316 [3, 4, 7, 11], while information on the evolution of the initial microstructure is still missing.

Beside the overall swelling, it is also important to examine how the dislocation cell structure locally influences the accumulation of irradiation-induced defects. The development of dislocation loops relative to the dislocation cells have been studied with *in-situ* TEM [5, 6]. Those *in-situ* experiments did not

reveal the formation of voids, which may have been due to the foil surface effect and relatively low dose. On the other hand, the high-dose *ex-situ* ion irradiation revealed void formation at high temperatures, indicating some heterogeneity of void distribution where either suppressed or enhanced void formation was observed near preexisting cell boundaries depending on irradiation conditions [3, 7]. Whether the controlling factor is the dislocation sink density, strain field, elemental segregation, precipitates, or some other variable remains unclear.

As a confounding factor, the dislocation cell structure is itself influenced by irradiation. *In-situ* ion irradiation studies showed that, in general, as irradiation-induced defects accumulated, the dislocation cell structures gradually became less and less apparent due to dislocation climb and interactions between loops and dislocations [5, 6]. In addition, Shang et al. showed that elemental segregation and precipitation can still be observed in the initial dislocation cell walls after irradiation at 400°C to 5 dpa, indicating that the coevolution of dislocations, segregation and precipitations of the dislocation cell structures need to be investigated individually. Nevertheless, data from *ex-situ* irradiations at lower doses relevant to operational doses are lacking.

This work presents the characterization of *ex-situ* and *in-situ* ion-irradiated laser powder bed fusion (LPBF) 316L and LPBF 316H SS to understand the initial damage evolution as a function of dose, temperature and carbon concentration, focusing on the evolution of irradiation-induced defects such as dislocation loops, voids, precipitates, and hardening and the role of the initial dislocation cell structure affecting the degradation process.

2 EXPERIMENT

2.1 Materials and pre-irradiation specimen preparation

Two materials were investigated in this study: as-built LPBF 316L and as-built LPBF 316H SS. The compositions are given in Table 1 along with the ASTM specification for 316L and 316H [26]. The L and H denotes low and high carbon, respectively. The LPBF 316L was printed at Oak Ridge National Laboratory (ORNL) using a GE Concept Laser M2 system, and the composition and printing parameters of the as-built material are provided as the powder feedstock composition provided by the vendor [10]. The LPBF 316H was printed at Argonne National Laboratory (ANL) using a Renishaw AM400 system [27]. The powder composition was provided by the vendor. The print composition of LPBF 316H was measured by cutting a small piece from the build and analyzed with the combustion infrared detection for carbon, inert gas fusion for hydrogen, oxygen and nitrogen, and direct current plasma emission spectroscopy for other elements.

The printed materials were machined into 3 mm-diameter rods via electrical discharge machining

Table 1. Composition of the AM materials (wt%)

Materials	LPBF 316L (Powder)	316L (ASTM A240)	LPBF 316H (Powder)	LPBF 316H (Print)	316H (ASTM A240)
Oxygen	0.05	-	0.05	0.046	-
Nitrogen	0.01	-	0.01	0.015	-
Carbon	0.006	<0.03	0.05	0.04	0.04-0.1
Sulfur	-	0.03	-	0.005	0.03
Iron	Bal.	Bal.	Bal.	Bal.	Bal.
Chromium	17.1	16-18	17.6	17.04	16-18
Manganese	1.19	2	1.03	1.09	2
Silicon	0.46	0.75	0.41	0.45	0.75
Nickel	12.1	10-14	12.3	12.22	10-14
Copper	0.01	-	-	0.007	-
Molybdenum	2.41	2-3	2.6	2.57	2-3
Vanadium	-	-	-	0.01	-
Phosphorus	<0.005	0.045	<0.005	0.018	0.045
Cobalt	0.1	-	-	0.028	-
Tungsten	-	-	-	<0.002	-

(EDM) along their build directions. Then, the rods were cut into 0.5 mm-thick disks via EDM or 0.6-1 mm-thick disks via a slow speed saw. For *in-situ* ion irradiations, the disks were mechanical polished on both sides with sandpapers from 400 grit to 800 grit to a thickness around 100 µm, and then electropolished at a temperature between -30ºC and -40ºC until perforation using a Struers Tenupol-5 polisher. The electrolyte was composed of 5% perchloric acid and 95% methanol. For *ex-situ* ion irradiations, only one side of the disks was polished. The polishing was performed with sandpapers down to P4000 grit, polycrystalline diamond suspension down to 1 µm, vibratory polishing using 50 nm colloidal silica polishing suspension, and finally electropolishing at -30ºC to -40ºC using the same electrolyte for 20-30 seconds. The dislocation densities of the two materials have been measured previously with x-ray using modified Williamson-Hall method [28–30].

2.2 *Ex-situ* ion irradiation

Ex-situ ion irradiations were performed on LPBF 316L and LPBF 316H with 4 MeV Ni^{2+} ions at 300°C and 600°C to 0.2, 2, 5 and 10 dpa using a Tandem accelerator in the Intermediate Voltage Electron Microscope (IVEM)-Tandem facility at ANL. The ion beam was bent through a magnet before entering the specimen chamber, and slightly rastered to ensure a uniform flux on the sample. The rastering frequencies are 1,000 Hz in horizontal direction and 10,000 Hz in vertical direction. The rastering amplitude is about 5% of the beam size. The dosimetry was composed of a (rear) Faraday cup behind the specimen and a (front) annular Faraday cup in front of the specimen. The beam current through the 3 mm diameter aperture was measured by the rear Faraday cup before, after, and if necessary, during the irradiation if the beam conditions changed. When the beam was on target, the current was monitored and integrated with the front annular cup. The flux of the beam was 1.72×10^{12} ions/cm^2/s, which corresponds to current readouts of 39 nA on the rear Faraday cup. Based on the SRIM calculation [31](Fig. 1a), which was performed using Co-58 instead of Ni-58 due to an error in the SRIM database for Ni-58, this flux results in a dose rate of 10^{-3} dpa/s at a depth of 400 nm, the same depth where the dose (dpa) of

each specimen was calculated. During irradiation, the current readout on the annular Faraday cup was monitored for beam stability.

For each *ex-situ* ion irradiation, the 3 mm specimen was clamped in a stainless steel holder. The sample was held in place by a Ta disk backed by a set screw. The sample holder was attached to a heating block containing a 400 watt quartz halogen lamp. A type K thermocouple was attached to the surface of the sample holder for temperature measurement. The irradiation chamber was pumped by an ion pump as well as by a magnetically levitated turbo pump backed by a scroll pump. Vacuum, measured with an ion gauge, varied between the mid 10^{-8} Torr range for 300°C irradiations and the low 10^{-7} Torr range for 600°C irradiations.

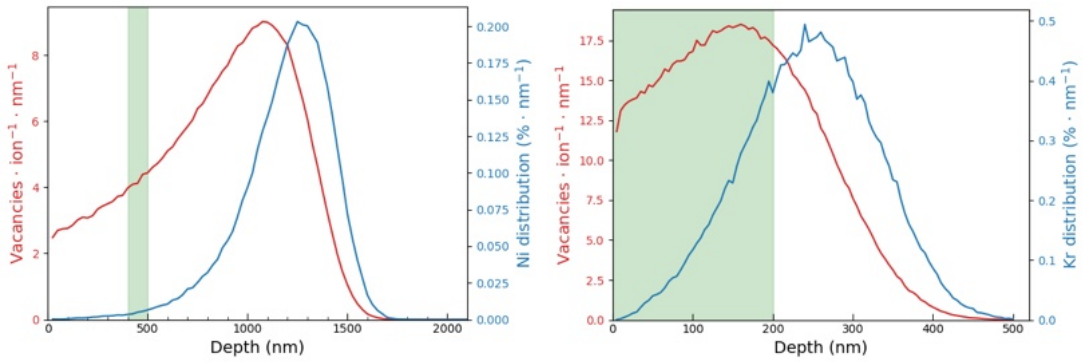

(a) 4 MeV Co ions **(b)** 1 MeV Kr ions

Figure 1. SRIM calculation of the displacement damage and implantation distribution of (a) 4 MeV Co^{2+} ions (simulating 4 MeV Ni^{2+} ions) and (b) 1 MeV Kr^{2+} ions into Type 316 stainless steels. The green area indicates the depth range of TEM examination.

2.3 *In-situ* ion irradiation

In-situ ion irradiations were performed at the IVEM-Tandem Facility using a NEC implanter and a Hitachi-9000 TEM [32]. The ion beam was bent through a magnet and a deflector before entering the microscope with an angle of 30° away from the electron optical axis. The microscope was operated at 300 kV to provide electron transparency for the thicker region of the specimen foil. The vacuum, which was measured with a cold-cathode gauge positioned near the specimen holder, was maintained between 5×10^{-8} to 3×10^{-7} Torr. A Gatan double-tilt heating holder (model 652) was used to control the specimen temperature and tilt the specimen to the desired crystalline orientation. During irradiation, the specimen holder was tilted about 15° toward the ion beam. Before irradiation, the current was measured using a Faraday catch cup located about 5 cm above the sample. The ion flux was calculated by dividing this current by the size of the limiting aperture positioned upstream. During irradiation, the catch cup was removed, and the current was monitored using a skim cup placed between the sample and the limiting aperture. The ion beam was slightly rastered, with a setting similar to that of *ex-situ* ion irradiation, to

achieve a uniform intensity across the irradiation area.

Kr^{2+} ions with an energy of 1 MeV and a flux of 6.3×10^{11} ions/cm^2 were used. This flux corresponds to a dose rate of 10^{-3} dpa/s, as calculated by SRIM [31] at a depth of 100 nm in quick calculation mode (Fig. 1b). The irradiation was paused to take images and diffraction patterns at designated dose steps. Bright-field (BF) and dark-field (DF) images were taken in two beam conditions with g = 200 near the 011 or 001 zone axes. Dislocation loops typically have an elliptical shape and the length of the long axis is taken as the size. Cavities and precipitates were imaged in BF with defocused conditions. They are typically circular and the diameter is taken as the size. For experiments with irradiation temperatures above 500°C, the temperatures were reduced to 250-350°C during image acquisition. This reduced the thermal annealing effect on the irradiation-induced defects and the potential oxidation on foil surface and enhanced the image quality. The end fluence is 3.1×10^{15} ions/cm^2 (5 dpa). Images for the end fluence were taken at room temperature.

2.4 Microhardness measurement of as-built materials

The microhardness of as-built LPBF 316L and LPBF 316H was measured with a Buehler Micromet using a 50 g load. Each material underwent 9 indents with a 250 μm spacing and a 10-second dwell time. Prior to microhardness measurements, specimens were hot-pressed mounted in conductive phenolic compound, followed by mechanically polishing with abrasive papers to P4000 grit, diamond suspension to 1 μm, and finally vibratory polishing with 50 nm colloidal silica.

2.5 Post-irradiation nanoindentation and microstructure characterization

Before preparing the TEM specimens of *ex-situ* irradiated samples, nanoindentation was performed with a Bruker TI Premier with a Berkovich tip on as-built and *ex-situ* irradiated specimens. The irradiated specimens were mounted on Ted Pella AFM specimen disks with CrystalBond™ as an adhesive. Before the measurements, a tip-area function was measured on fused quartz to ensure that the calibrated hardness and the reduced modulus of fused quartz was 9.25±10% GPa and 69.6±5% GPa, respectively. Eighty-one indents were performed with decreasing load from 10,000 μN to 500 μN. A load pattern of 5-2-5 (5 sec for ramp-up, 2 sec for hold, and 5 sec for ramp-down) was used for all indents. The hardness-vs.-contact depth data was fitted to a 3rd order polynomial function and the value at 200 nm was reported as the hardness of the sample and the root mean square error is reported to be consistent across the specimens for semi-quantitative comparison. The high hardness suggests that the characteristic length, h*, should be less than 200nm [33], and the results will be only minorly influenced by the indentation size effect [34].

Following nanoindentation, the TEM specimens of the *ex-situ* irradiated specimens were prepared by electropolishing. First, lacquer was applied to cover about one-third of the irradiated surface from

the edge. After that, the specimens were electropolished using a power supply that gives a square pulse of constant voltage of 28 V to remove a depth of about 400 nm from the irradiated surface. A Bruker ContourGT optical profilometer was used to measure the precise depth removed. After flash polishing the irradiated side, lacquer was applied again to cover the whole irradiated side and electropolishing was performed again using a Struers Tenupol-5 from the unirradiated side until perforation. Attention was paid to ensure that the perforated region for TEM observation was significantly away from the location where nanoindentation was performed. In addition to electropolishing, one lamella was prepared from LPBF 316L irradiated at 600°C to 2 dpa using a Zeiss NVision FIB in the Center for Nanoscale Materials at ANL. The TEM imaging procedure for *ex-situ* irradiated specimens is similar to that for *in-situ* irradiation.

3 RESULTS

As a preface, the results including micrographs and associated descriptions are distributed between the article and supplemental materials to keep the article focused and concise.

3.1 Microstructural characterization and Vickers hardness of as-built materials

Fig. 2 and Supplemental Fig. S1 show TEM images of as-built LPBF 316L and LPBF 316H, respectively. Fig. 3 shows the high-angle annular dark field (HAADF) image and the corresponding EDS elemental maps of as-built LPBF 316H. Both materials exhibit a dislocation cell structure with nano-sized $MnSiO_3$ rhodonite phase [35] particles with an average size of 18.5 nm predominantly decorating the cell boundaries, as shown in Fig. 2c. The size of the dislocation cells is around 500 nm and the wall thickness is approximately 100 nm. Notably, dissociated dislocations labeled A in the DF images suggest that the stacking fault energies of these materials are low. As indicated by labels B in Fig. 2b, some small defects, likely dislocation loops, were observed. The Vickers hardness of the as-built LPBF 316L and LPBF 316H was 205±8 HV and 228±8 HV, respectively.

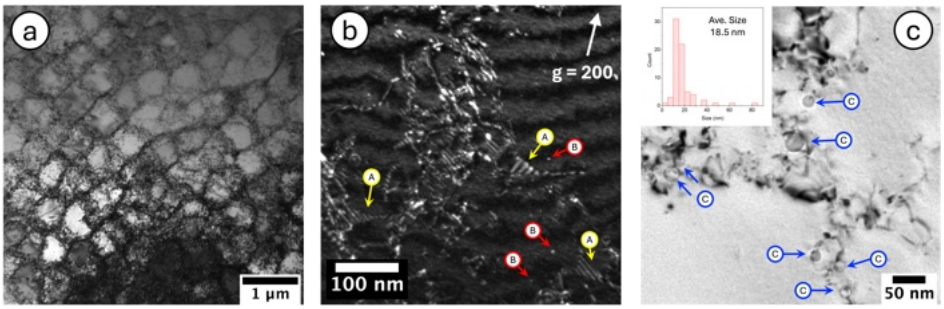

Figure 2. TEM images of as-built LPBF 316L: (a) low-magnification BF TEM image. (b) high-magnification DF TEM image in a two-beam condition with g = 200 near the 001 zone axis. The yellow A arrows highlight the dissociated partial dislocations. The red B arrows highlight defect clusters. (c) Underfocused BF TEM image with blue arrows C highlighting the $MnSiO_3$ precipitates. The inset shows the size distribution of the $MnSiO_3$ particles.

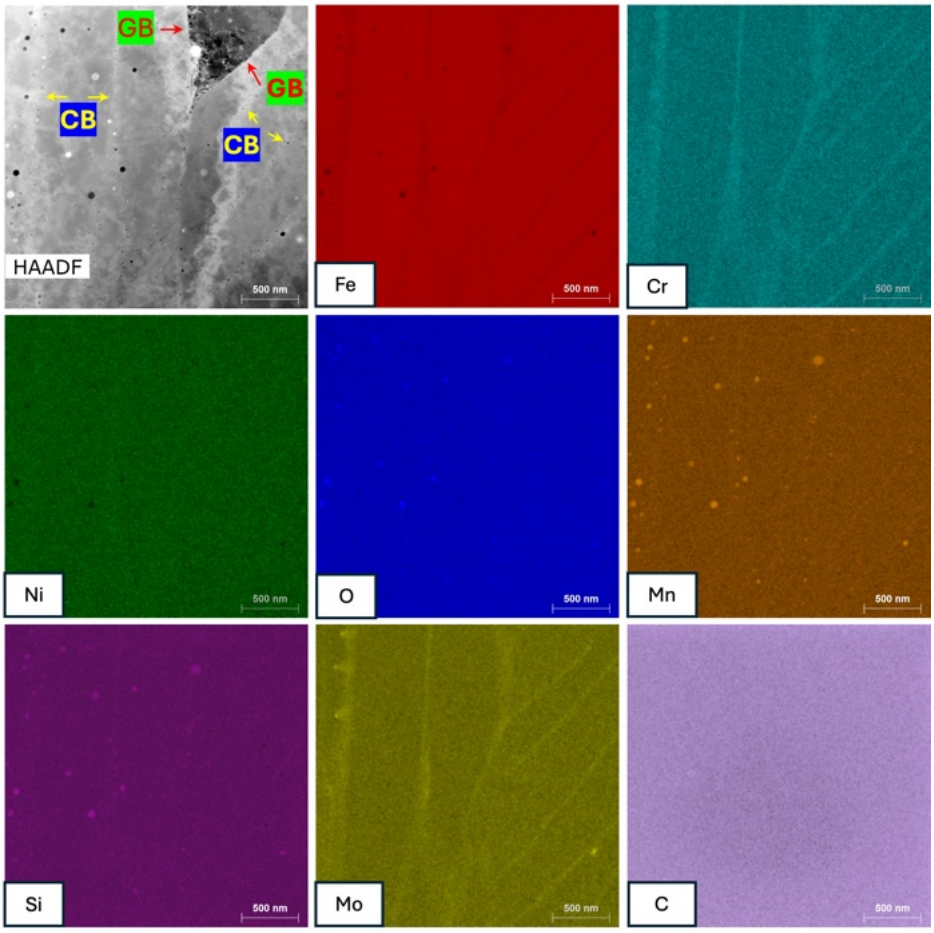

Figure 3. HAADF TEM image of as-built LPBF 316H and the corresponding EDS elemental maps. The labels GB and CB indicate grain boundary and cell boundary, respectively

Elemental maps of LPBF 316H are shown in Fig. 3, revealing enrichment of Cr, Mo, and marginal Si at both dislocation cell walls and grain boundaries, with depleted Fe, resulting from the fabrication process. $MnSiO_3$ rhodonite nanoparticles decorate the cell walls. No carbides nor carbon segregation were detected. The elemental maps of LPBF 316L can be found in a previous report [36]. The elemental distribution in LPBF 316H and LPBF 316L are similar and both aligns with previous findings in LPBF 316L [12]. The dislocation densities for as-built LPBF 316L and 316H are 2.3×10^{14} m^{-2} and 4.7×10^{14} m^{-2} [28, 29], respectively, which is about two orders of magnitude higher than typical wrought 316 SS.

3.2 Defect evolution observed with *ex-situ* ion irradiation

3.2.1 Stability of the dislocation cell structure

The stability of the dislocation cell structures in LPBF 316L and LPBF 316H under irradiation at 600°C as a function of dose is shown in Fig. 4 and Fig. 5, respectively. The original dislocation cell structures in LPBF 316L and LPBF 316H gradually evolved into a uniform dislocation network with increasing dose. For LPBF 316L irradiated to 0.2 dpa, the dislocation cell structure can still be observed in some

regions, as shown in Fig. 4a. However, the cell walls broadened and were less obvious as compared to those prior to irradiation. In other regions, dislocation distribution appears to be uniform and cell structure is no longer visible. Cell wall broadening has been previously observed in AM 316L *in-situ* irradiated at 400°C to 5.5 dpa [5]. Dislocation climb and de-tangling has been shown to increase the separation between the dislocations within the dense dislocation walls under irradiation [37]. Conversely, for LPBF 316H irradiated to 0.2 dpa, the dislocation cell structure is still visible with a morphology similar to the as-built condition. However, in other regions, as shown in Fig. 5a, the cell boundaries were transformed from high dislocation density regions into sharp boundaries characterized with Moiré fringes, as shown in the enlarged images of Fig. 5a, indicating the annihilation of dislocations at the dislocation cell walls. The different contrast between neighboring cells indicates the relative misorientation between them. Therefore, two mechanisms may be in operation in LPBF 316: cell wall broadening and dislocation annihilation. While the two mechanisms were observed individually in LPBF 316L and LPBF 316H, it is not certain if each mechanism is active only to the specific carbon concentration (LPBF 316L versus LPBF 316H) because those phenomena were observed within very limited sample volumes. A systematic survey of large areas of each material is still needed.

After irradiation at 600°C to 2 dpa, both materials exhibited a relatively uniform dislocation network, with the original cell walls mostly invisible. This observation further pushes the lower limit for the loss of dislocation cell structures from the 30 dpa cited in literature [3] to 2 dpa. Nevertheless, traces of the original cell structure can still be observed as contrast domains. Taking LPBF 316H in Figure 5b for example, the grain on the top is in a weak two-beam condition with g=200 near the [011] zone axis. The domain below the yellow dashed line exhibits stronger diffraction contrast than the surrounding areas, indicating an offset in crystal orientation. Additionally, its width is approximately 500 nm, further suggesting it is the original dislocation cell. Similar observation can be found in LPBF 316L, as shown in Supplemental Fig. S2. In other words, at 2 dpa, the original dislocation cell structure in both LPBF 316L and LPBF 316H has been replaced by a uniform dislocation network, but the misorientation between the cells has somewhat persisted. With further damage levels of 5 dpa and 10 dpa, as shown in Fig. 4(c-d) and Fig. 5(c-d), even the misorientation domains are no longer recognizable; the dislocation part of the dislocation cell structure has completely disappeared.

Fig. 6 and Fig. 7 present low-magnification images of LPBF 316L and LPBF 316H, respectively, irradiated at 300°C as a function of dose. At 0.2 dpa, as shown in Fig. 6a, LPBF 316L shows the introduction of dislocation loops and black-spot defects by irradiation, while the original dislocation cell structure remains visible. However, at doses of 2 dpa and above (Fig. 6b to 6d), dense defects appear, and the dislocation cell structure becomes indistinguishable from the other defect structures. In

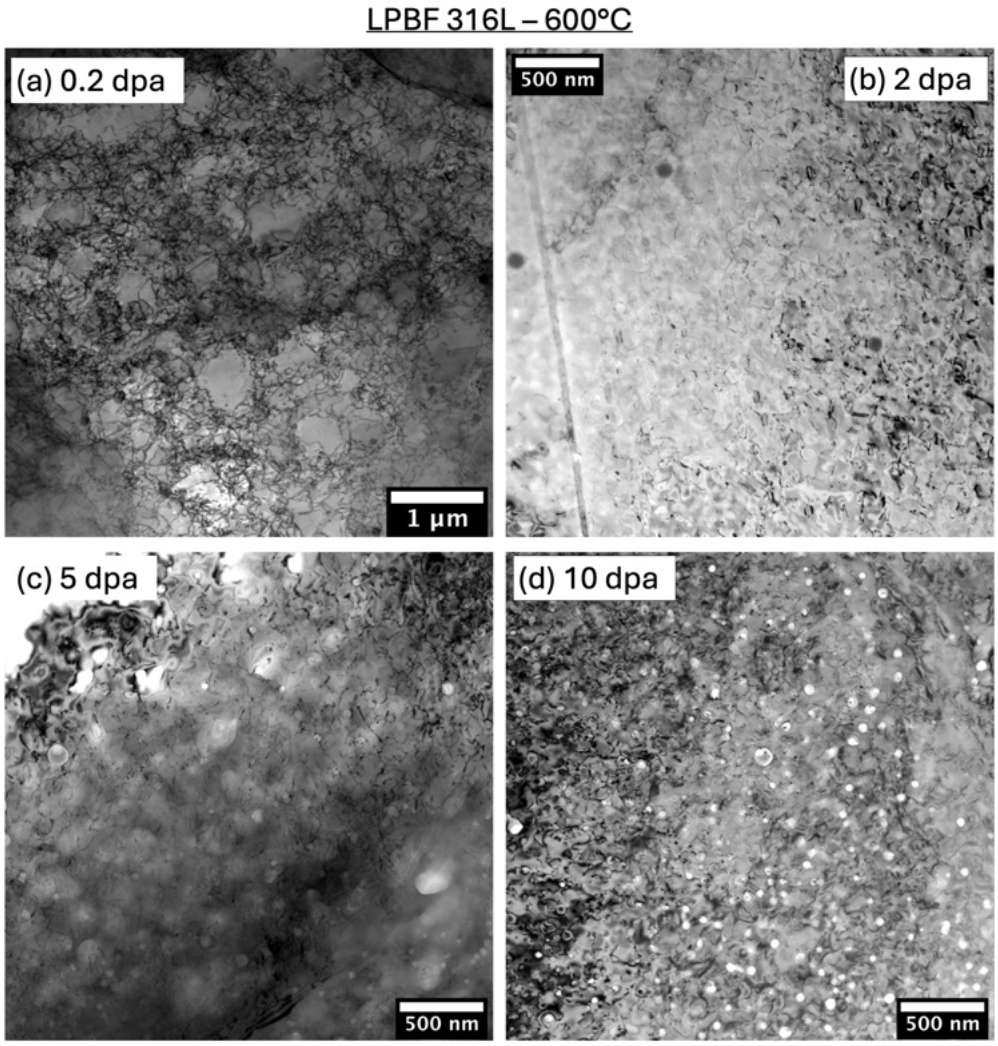

Figure 4. BF TEM images of LPBF 316L *ex-situ* irradiated with 4 MeV Ni^{2+} ions at 600°C to (a) 0.2 dpa, (b) 2 dpa, (c) 5 dpa and (d) 10 dpa.

contrast, Fig. 7a illustrates that LPBF 316H exhibits a much higher defect density at 0.2 dpa compared to LPBF 316L, with the original dislocation cell structure being more obscured. However, as demonstrated in Supplemental Fig. S3, a series of same-area images with varying contrast reveals that enhancing diffraction contrast can make the dislocation segments of the cell structure more apparent, confirming that dislocation cells remain at this dose level, albeit with potentially an altered dislocation density. As the dose increases further (Fig. 7b to 7d) the cell structure in LPBF 316H, like in LPBF 316L, is mostly replaced by irradiation-induced defects.

3.2.2 Voids

Very few voids were observed in 300°C *ex-situ* irradiated samples (Supplemental Figs. S4 to S6). At 0.2 dpa, no voids were detected in either LPBF 316L or 316H. In LPBF 316L, some small voids with an average size of 1.5 nm and a total calculated swelling of 0.00012% appeared at 2 dpa. At 5 dpa, voids

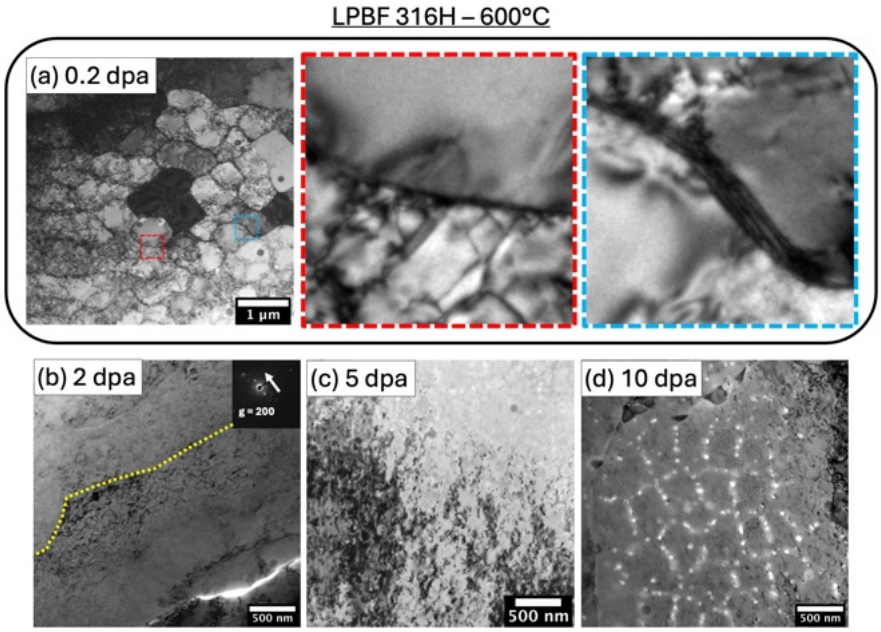

Figure 5. BF TEM images of LPBF 316H *ex-situ* irradiated with 4 MeV Ni^{2+} ions at 600°C to (a) 0.2 dpa, (b) 2 dpa, (c) 5 dpa and (d) 10 dpa. The red and blue boxes in (a) are enlarged images of cell boundaries.

with similar size still persisted, though their density decreased, and by 10 dpa, no voids were observed. In LPBF 316H, similar sized voids were detected at 2 dpa but at a significantly lower density than in LPBF 316L at the same dose. No voids were detected in LPBF 316H at 5 dpa and 10 dpa. At 600°C, no evident voids were observed in both materials up to 2 dpa (Supplemental Fig. S7). In contrast, for 5 dpa and 10 dpa at 600°C, faceted voids are evident in both materials, as shown in Fig. 8. The average void size as a function of dose is illustrated in Fig. 9a, where the size distribution of each condition is shown in Fig. 9d. In both materials, the void size increases with increasing dose. For LPBF 316L, the average void size increases moderately from 34 nm at 5 dpa to 39 nm at 10 dpa. In contrast, for LPBF 316H, the average void size at 5 dpa is 18.8 nm, significantly smaller than that of LPBF 316L. However, it increases markedly to 58.4 nm at 10 dpa, surpassing that of LPBF 316L at the same dose. The void density, as shown in Fig. 9b, also rises with increasing dose in both materials. Notably, LPBF 316L exhibits a higher void density at 5 dpa and a greater rate of increase in density from 5 dpa to 10 dpa compared to LPBF 316H.

It should be noted that the average void size of LPBF 316H irradiated to 5 dpa is 18.8 nm, which is comparable to the 18.5 nm size of the pre-existing $MnSiO_3$ particles (Fig. 2c). To confirm the presence of voids, EDS mapping was conducted, as illustrated in Fig. 10. For instance, the feature highlighted within the red box in the HAADF image shows a lower X-ray intensity for all elements at its center, indicating the presence of a void. Additionally, a layer of Ni and Si enrichment was observed surrounding the void,

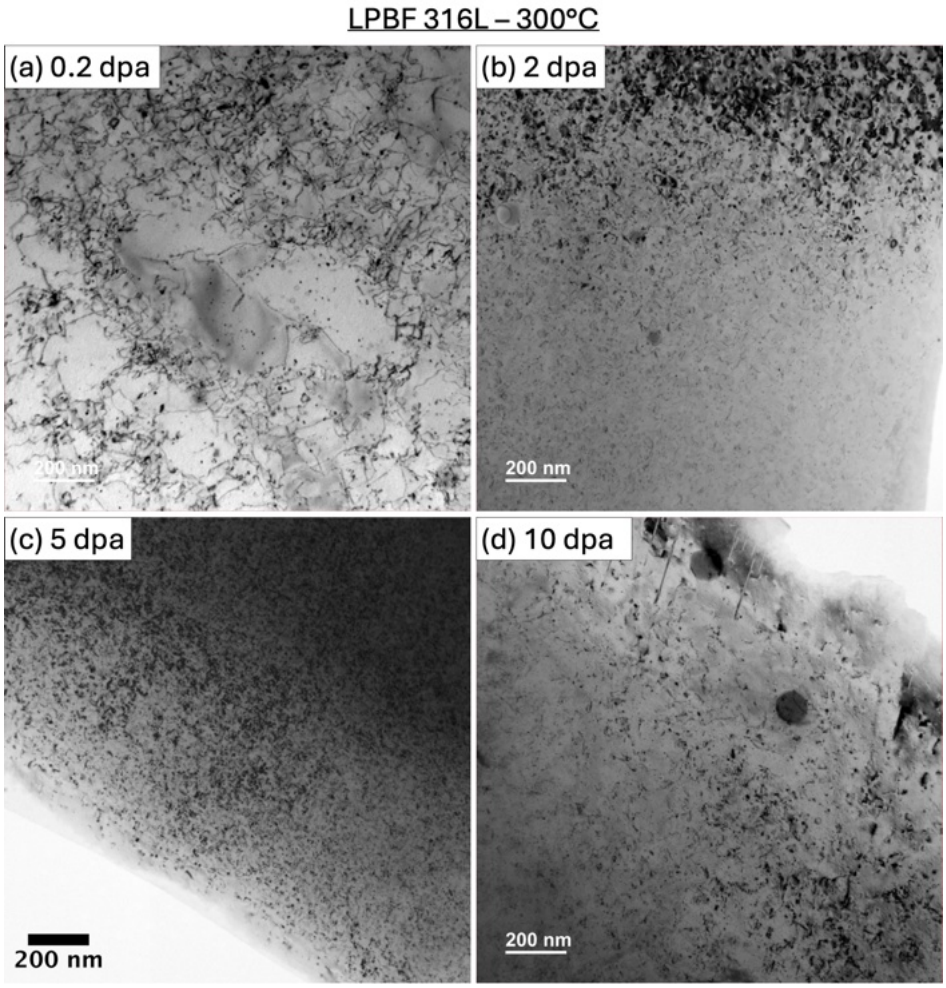

Figure 6. BF TEM images of LPBF 316L *ex-situ* irradiated with 4 MeV Ni^{2+} ions at 300°C to (a) 0.2 dpa, (b) 2 dpa, (c)5 dpa and (d) 10 dpa

which is attributed to radiation-induced segregation (RIS). Similar Ni enrichment around voids is observed in the 10 dpa sample, as shown in Fig. 11. In contrast, while Si enrichment can still be observed around some voids, Si enrichment is absent around some other voids (e.g., the red box). In some cases (e.g. the blue box), Si enrichment appears as precipitates adjacent to, rather than surrounding, the voids.

The total swelling as a function of dose is shown in Fig. 9c. The swelling increases with increasing dose with a rate of 0.54%/dpa for LPBF 316L and 0.49%/dpa for LPBF 316H. Assuming an linear dependence, the onset dose for swelling is backward estimated to be 3.5 dpa and 4.9 dpa for LPBF 316L and LPBF 316H, respectively. The projected onset dose of LPBF 316L of 3.5 dpa is consistent with the observation that voids are absent at 2 dpa (Fig. S8). On the other hand, the onset dose for LPBF 316H of 4.9 dpa indicates that the LPBF 316H had just started to swell at 5 dpa, which is consistent with its small voids (Fig. 8c). The higher swelling in LPBF 316L at 5 dpa and 10 dpa is primarily due to its shorter incubation time, and marginally due to the higher swelling rate. In addition, although LPBF 316H

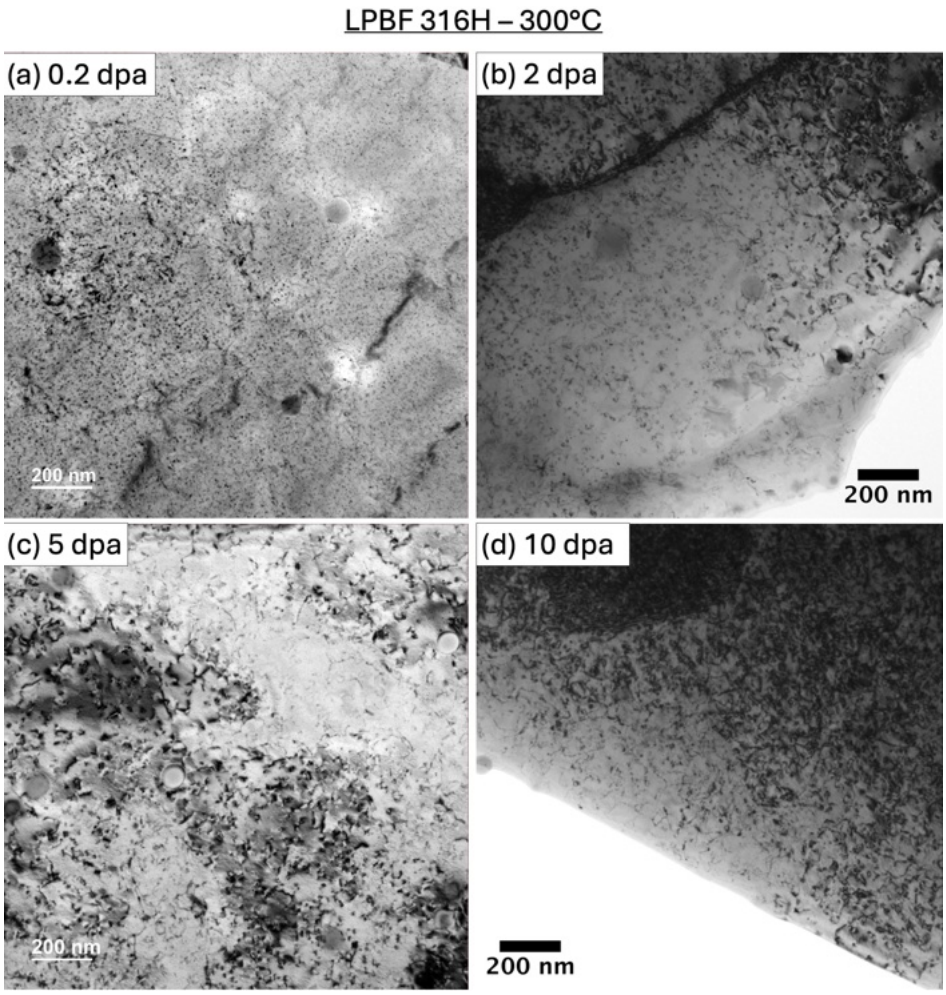

Figure 7. BF TEM images of LPBF 316H *ex-situ* irradiated with 4 MeV Ni^{2+} ions at 300°C to (a) 0.2 dpa, (b) 2 dpa, (c) 5 dpa and (d) 10 dpa

has a higher void growth rate than LPBF 316L, it is compensated for by its much lower nucleation rate, resulting in its lower total swelling at both 5 dpa and 10 dpa compared to LPBF 316L.

Another observation about the void formation in LPBF 316L and LPBF 316H is the heterogeneous distribution of voids. As shown in Fig. 8b and Fig. 8d, voids were observed within cell structures, likely along the original dislocation cell boundaries, accompanied by Ni-Si-rich precipitates at 5 dpa and Ni-rich precipitates at 10 dpa. This is notable because the dislocation cell structure had already transitioned to a uniform dislocation network by 2 dpa (Fig. 4b and Fig. 5b). Interestingly, voids were found at the prior dislocation cell boundaries, but not at the grain boundaries.

3.2.3 Dislocation loops and small defects

Irradiation at 600℃ The formation and evolution of irradiation-induced dislocation loops in LPBF 316L and LPBF 316H irradiated at 600°C is shown in Fig. 12 and Fig. 13, respectively, including the corresponding size distribution where the faulted, perfect and undetermined loops are colored in blue,

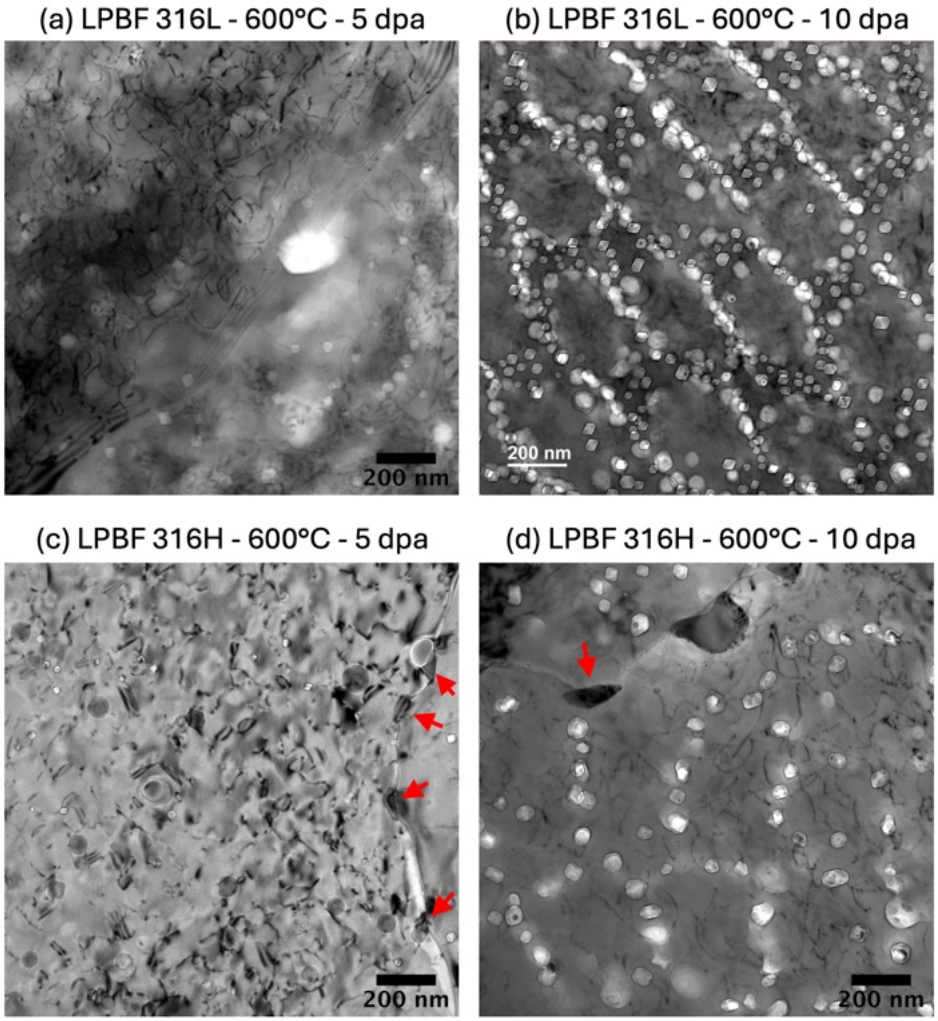

Figure 8. BF TEM images of (a, b) LPBF 316L and (c, d) LPBF 316H irradiated with 4 MeV Ni^{2+} ions at 600°C with a dose rate of 10^{-3} dpa/s. (a, c) at 5 dpa; (b, d) at 10 dpa. Images are taken in an under-focused condition with a defocused amount from 1.5 μm and 5 μm. The red arrows indicate $M_{23}C_6$ carbides at the grain boundaries.

orange and green, respectively. At 0.2 dpa, both LPBF 316L and LPBF 316H exhibit very few large dislocation loops. In LPBF 316L, small features, as highlighted with the red arrows in Fig. 12, were observed with an average size of 3.7 nm (SD = 0.76 nm). Initially appearing as "black spots" defect clusters, higher magnification images at 500kx, shown in the inset, reveal Moiré fringes, indicating these features are precipitates. These precipitates were not present before irradiation, and are significantly smaller than the pre-existing $MnSiO_3$ particles, which have an average size of 18 nm, suggesting that they were introduced by the 600°C irradiation. The LPBF 316H, on the other hand, does not appear to exhibit such tiny precipitates.

At 2 dpa and 5 dpa, both materials exhibit large dislocation loops. Faulted loops and perfect loops can be distinguished by their shape and internal fringes, along with smaller loops whose type were not

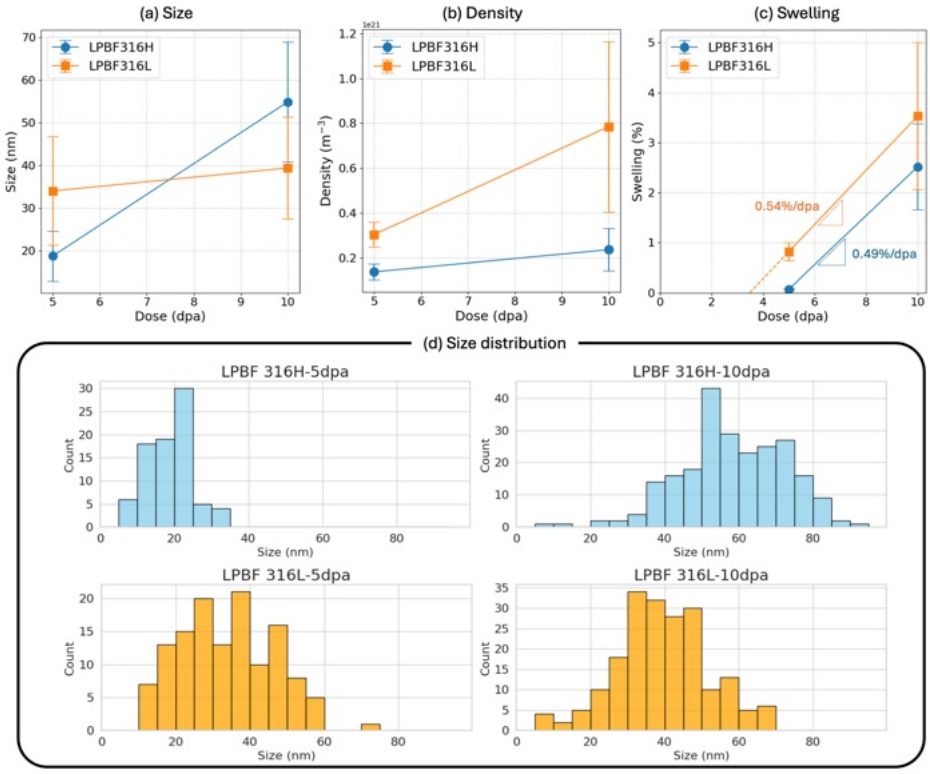

Figure 9. The (a) average void size and size distribution, (b) void density, (c) total swelling and (d) void size distribution observed in LPBF 316L and LPBF 316H irradiated at 600°C with 4 MeV Ni^{2+} ions as a function of dose. The units of the x and y axes of the size distribution is nm and count, respectively. The dashed line in (c) is a backward extrapolation based on the two data points at 5 dpa and 10 dpa. The error bar is the standard deviation.

determined. As shown in Fig. 13, faulted loops (indicated by yellow arrows) are more abundant and larger in size compared to perfect loops (e.g., blue arrow in Fig. 13d). Supplemental Table S1 shows that faulted loops are approximately 3 to 4 times more prevalent than perfect loops at 2 dpa and 5 dpa. Due to insufficient data, reliable ratio measurements for 0.2 dpa and 10 dpa are not available.

Fig. 14 shows the size and density measurements for dislocation loops larger than 5 nm. In general, the two materials follow similar trends. At 600°C, the loop size in both materials peaks at 2 dpa and then decreases as the dose increases to 10 dpa. For LPBF 316H, the loop density increases with increasing dose up to 2 dpa, decreases slightly at 5 dpa, and then declines sharply at 10 dpa. For LPBF 316L, on the other hand, the loop density also peaks at 2 dpa, but its reduction with increasing dose is more gradual. Between the two materials, the average loop size and density are consistently larger in LPBF 316H compared to LPBF 316L from 0.2 dpa to 5 dpa. By 10 dpa, large dislocation loops become scarce in LPBF 316H, whereas they remain observable in LPBF 316L, as shown in Fig. 12(k).

Both interstitial- and vacancy-type dislocation loops can form in irradiated austenitic SS. Shang et al. observed a mixture of both types of loops in AM316LN irradiated with 3.5 MeV Fe ions at 450°C

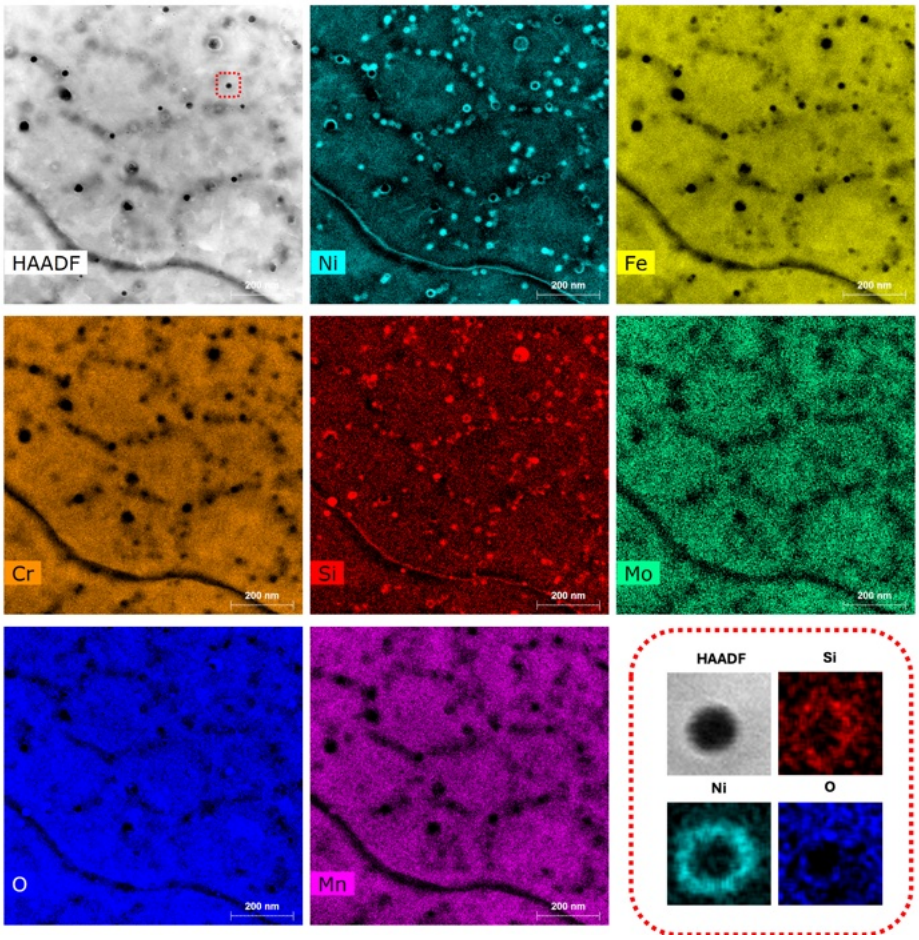

Figure 10. EDS intensity maps of LPBF316H irradiated at 600°C with 4 MeV Ni^{2+} ions to 5 dpa. The enlarged elemental maps of the void in the red box in the HAADF image are shown in the lower-right corner.

to a peak dose of 220 dpa [11]. In contrast, Loyer-Prost et al. reported predominantly interstitial-type dislocation loops in AM 316 SS irradiated at 550°C with 5 MeV Fe ions to 3 dpa [9]. The difference between the two studies aligns with earlier findings where the fraction of interstitial loops increases with increasing irradiation temperatures [38]. Based on this trend, the dislocation loops observed in our study at 600°C are expected to be predominantly interstitial in nature. The smaller loop enclosed within a larger one in Fig. 13h may present the rare case of vacancy loop, similar to the features reported by Loyer-Prost et al. [9]. In contrast, loops observed at 300°C in our study, which will be discussed in next section, could include a mixture of both types.

Fig. 14c illustrates the number of defects, being either interstitials or vacancies, contained in dislocation loops as a function of dose. Both materials exhibit peak retention at 2 dpa at 600°C, followed by a decrease with increasing dose. Up to 5 dpa, more defects are retained in dislocation loops in LPBF 316H compared to LPBF 316L, but this trend reverses at 10 dpa mostly due to the decline of loop density in LPBF 316H.

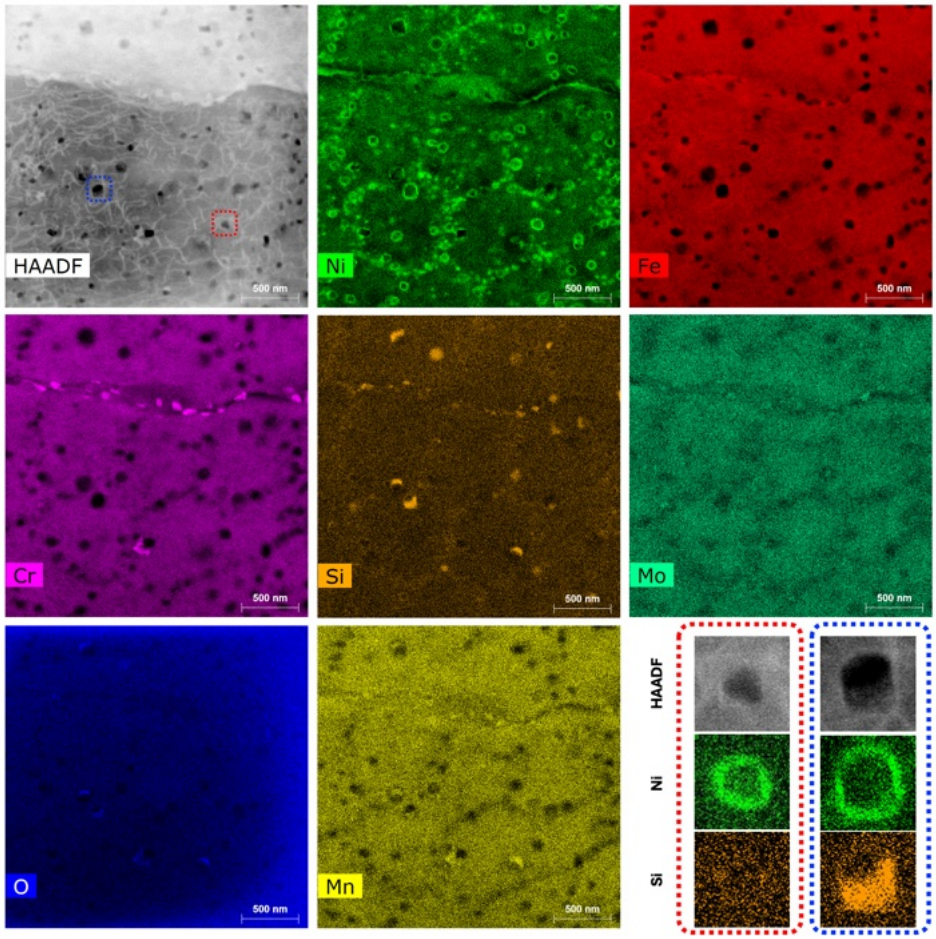

Figure 11. EDS intensity maps of LPBF316H irradiated at 600°C with 4 MeV Ni^{2+} ions to 10 dpa. The enlarged elemental maps of the void in the red and blue boxes in the HAADF image are shown in the lower-right corner.

In addition to the large dislocation loops, small black-spot defects are observed with a low density in the 10^{19} m^{-3} range. Most of these black-spot defects do not have a triangular shape, indicating they are likely small dislocation loops. The lack of SFT at 600°C is consistent with the fact that this irradiation temperature is much higher than the stage V temperature of stainless steels, 300°C, where SFT become unstable [39, 40]. In only LPBF 316H irradiated to 0.2 dpa, some SFT were observed, as shown in Fig. 15. Interestingly, SFT near the grain boundary of this sample (Fig. 15b) appear larger than those inside the grain (Fig. 15a), suggesting a supersaturation of vacancies near the grain boundary [41].

Irradiation at 300℃ Fig. 16 and Fig. 17 show the high-magnification BF and DF images, and the corresponding diffraction patterns of LPBF 316L and LPBF 316H, respectively, irradiated at 300°C. The defect size distributions for 0.2 dpa and 10 dpa are shown in Fig. 18. At this temperature, the defect microstructure is composed of a high density of defects smaller than roughly 3 nm (dislocation loops or SFT) and a significantly lower density of larger, resolvable dislocation loops.

In LPBF 316L irradiated to 0.2 dpa (Fig. 16a to c), faulted loops, perfect loops, and small black-spot defects are observed. Some black-spot defects are identified as SFT. As shown in Fig. 16(b1) and 16(b2), two orientations of SFT are observed, with their tips pointing in opposite directions along the [100] direction of the diffraction pattern seen in Fig. 16c. Other black-spot defects, such as the one depicted in Fig. 16(b3), do not exhibit the triangular shape characteristic of SFT and might be dislocation loops. It is noteworthy that these black-spot defects lack the Moiré fringes observed in LPBF 316L irradiated to 0.2 dpa at 600°C (Fig. 12), suggesting that they are not precipitates.

As the dose increases to 2 dpa, faulted loops, perfect loops, SFT, and non-SFT small defects remain present. The size of the large loops ($>$ 5 nm) increases, while the size of the SFT and other black-spot defects remains largely unchanged. The appearance of the rel-rod diffraction streak in Fig. 16f aligns with the observed increase in the number of faulted loops at this dose. Some faulted loops appear faceted. As the dose increases to 5 dpa and 10 dpa, the size of SFT and small loops persist with their size largely unchanged, while their density intensifies, particularly at 10 dpa, making it more challenging to characterize the large dislocation loops. Nevertheless, faulted loops are still present, as indicated by the edge-on loops highlighted by yellow arrows in Fig. 16h and Fig. 16k. As shown in Fig. 14a, the average size of large loops appears to be unchanged or even slightly decreased from 2 to 10 dpa. The loop density peaks at 5 dpa, as shown in Fig. 14b.

Magnified images of LPBF 316H irradiated at 300°C are shown in Fig. 17. At 0.2 dpa, LPBF 316H exhibits a significantly higher density of dislocation loops compared to LPBF 316L. However, as shown in Fig. 18a and Fig. 18c, LPBF 316H contains only smaller dislocation loops, while LPBF 316L shows some larger diameter loops, albeit at a relatively low density. The small loop size in LPBF 316H at this dose makes it difficult to determine the loop type. Nevertheless, the presence of edge-on loops observed along the [110] zone axis confirms the existence of faulted loops. Another distinction is that there is no clear evidence of SFT in LPBF 316H at 0.2 dpa in contrast to LPBF 316L.

With an increase in dose to 2 dpa, the dislocation loop size in LPBF 316H grows, coexisting with black-spot defects, some of which are identified as SFT, as shown in Fig. 17(e1) and (e2), and some, like the one in Fig. 17(e3), are dislocation loops. The appearance of rel-rod streaks in Fig. 17f indicates an increased population of faulted loops. As the dose increases to 5 dpa and 10 dpa, the average size of large dislocation loops ($>$ 5nm) continues growing, as shown in Fig. 14a, with faulted loops identifiable as edge-on loops, as highlighted by the yellow arrows in Fig. 17(g, h, i, k). The density of large dislocation loops peaks at 2 dpa, which is at a lower dose as compared with LPBF 316L, and then slowly declines, as shown in Fig. 14b.

3.2.4 Phase stability

Fig. 3, 19, 10 and 11 show the EDS intensity maps of LPBF 316H before irradiation and after irradiation at 600°C to 2 dpa, 5 dpa and 10 dpa, respectively. Cr and Mo enrichment observed at dislocation cell boundaries prior to irradiation remains visible at 2 dpa, but is no longer present at 5 dpa and 10 dpa. As briefly mentioned in Section 3.2.2, Ni-Si-rich precipitates are observed. As shown in Fig. 19, at 2 dpa, tiny Ni-Si-rich precipitates appear at high density with a relatively uniform distribution. Some of these precipitates exhibit a core-shell structure, with Si forming the core and Ni the shell, as shown in the enlarged Ni and Si maps.

As the dose increased to 5 dpa, the size of Ni-Si-rich precipitates increases, as shown in Fig. 10. Additionally, their distribution becomes more heterogeneous, mainly residing along the original dislocation cell walls and coexisting with irradiation-induced voids, as presented previously in Section 3.2.2. Potential phases containing Si and Ni in irradiated 316 SS include G-phase ($M_6Ni_{16}Si_7$), γ' (Ni_3Si) and phosphide [42]. Phosphide can be ruled out as they typically have a needle-like morphology, and contain phosphorous, which is not clearly detected in the EDS maps. G-phase, where M is primarily Mn and Cr [43], may also be excluded due to the lack of Mn enrichment as shown in Fig. 19 and 10. Therefore, the observed Ni-Si-rich precipitates at 2 dpa and 5 dpa were most likely γ' precipitates, consistent with previous reports in both wrought and AM 316L irradiated at 360°C to 2.5 dpa [44, 45] and AM316L irradiated at 600°C to 100 dpa [3].

When the dose was further increased to 10 dpa, as illustrated in Fig. 11, these precipitates at the cell walls persist but appear smaller in size. Ni enrichment is still evident in these small precipitates; however, the Si enrichment observed in the 2 dpa and 5 dpa samples is not as obvious. Further effort to understand why these Ni-Si-rich precipitates at 2 dpa and 5 dpa transformed to the Ni-rich precipitates at 10 dpa is still required.

Besides Ni-Si-rich precipitates, the formation of carbides at grain boundaries was examined. The carbides were presumably $M_{23}C_6$ rather than M_6C, as they did not exhibit clear Ni enrichment typically observed in M_6C precipitates in 316 stainless steels [42, 46, 47]. X-ray analysis will be needed to conclusively determine their nature. LPBF 316L shows no carbides for all irradiation conditions, as seen in Supplemental Fig. S8. This absence of carbides is reasonable given the alloy's low carbon content. Similarly, LPBF 316H irradiated at 300°C also exhibits no carbide formation at grain boundaries up to 10 dpa (Supplemental Fig. S9), likely due to the low diffusivity at this temperature. In contrast, carbides are observed for all doses, even 0.2 dpa, in LPBF 316H irradiated at 600°C, as shown in Fig. 20. Fig. 19 and Supplemental Fig. S10 show EDS maps near the grain boundaries in LPBF 316H irradiated to 2 dpa and 5 dpa, respectively, confirming the enrichment of Cr and C in the carbides. Oxygen enrichment at the

carbides were observed, however it is not clear if it is due to the reaction of carbides with the oxygen of the material, or with the oxygen in air or electrolyte during the electro-polishing process. The size and size distribution of the carbides, measured as the equivalent diameter of the area, is shown in Fig. 21, which suggests continuous growth in size with increasing dose. The density and volume fraction of these carbides require further investigation. The EDS maps indicate that carbides preferentially form at grain boundaries rather than at cell boundaries.

3.2.5 Nanoindentation

Fig. 22 presents the nanohardness measurements for LPBF 316L and LPBF 316H irradiated with 4 MeV Ni^{2+} ions at both 300°C and 600°C. Both materials exhibit higher hardness after irradiation at 300°C compared to after irradiation at 600°C. For LPBF 316L irradiated at 300°C (Fig. 22a), the hardness increases rapidly with the dose up to 5 dpa, after which it gradually decreases as the dose continues to rise up to 10 dpa. In contrast, at 600°C, the hardness initially decreases with the dose up to 2 dpa and then slowly increases with further irradiation up to 10 dpa. A similar trend is observed for LPBF 316H (Fig. 22b). At 300°C, the hardness increases sharply up to 2 dpa, followed by a decline with higher doses. At 600°C, softening occurs at low doses up to 2 dpa, after which the hardness gradually increases with increasing dose.

Comparing the two materials, as shown in Fig. 22c, LPBF 316H has a higher initial hardness than LPBF 316L. At 300°C, both materials exhibit significant hardening followed by softening as the dose increases. LPBF 316H reaches its peak hardness at a lower dose (2 dpa) compared to LPBF 316L (5 dpa). At 600°C, both materials initially soften and then harden with increasing dose, as shown in Fig. 22d. The initial softening under irradiation at 600°C is consistent with neutron data [10]. The more pronounced hardening in LPBF 316H at 600°C is likely due to the formation of $M_{23}C_6$ carbides.

3.3 Defect evolution observed with *in-situ* ion irradiation

The *in-situ* observation of defect evolution in LPBF 316H under irradiation at 600°C is shown in Fig. 23. Dislocation loops initially formed near the center of the dislocation cells, which were defect-free before irradiation as shown in Fig. 23a. The *in-situ* observation also indicates that once the irradiation started, the dislocations within the cell wall began to move and straighten, suggesting a decrease in the dislocation density. As the irradiation dose increased (Fig. 23b and 23c), these loops grew in size and filled the cell interiors, while the preexisting cell walls became thinner and eventually indistinguishable. Both perfect loops and faulted loops were observed with comparable size and density. The interactions between dislocation loops were insignificant by 1 dpa. By 3 dpa (Fig. 23d), dislocation loops had occupied the entire cell interior, and at 5 dpa (Fig. 23e), the interactions between loops led to the formation of a uniform dislocation network, replacing the original heterogeneous dislocation cell structure. This

evolution suggests that the dislocation cell structure strongly influences loop formation at this temperature.

Further analysis was conducted on the loop density and size. Due to the influence of surface effects during *in-situ* experiments at high temperatures, defects were analyzed as a function of foil thickness [48, 49] where electron energy loss spectroscopy (EELS) was employed to measure the foil thickness at various locations of *in-situ* observation, as shown in Supplemental Fig. S11. No large loops were formed in areas with a foil thickness less than $\sim$200 nm even up to 5 dpa, suggesting a denuded zone of approximately 100 nm from either side of the foil surface at 600°C. Therefore, the loops observed in Fig. 23 are likely concentrated in the middle of the foil, within a depth of only about 20 nm, representing practically a single layer of loop agglomeration.

In regions thicker than 200 nm, large loops can be observed and the measurements are illustrated in Fig. 24 as a function of dose. The loop size, measured as the average size of all loops observed, increases with increasing dose, with growth appearing to saturate between 3 and 5 dpa, as shown in Fig. 24a. The box in the Fig. 24 displays the interquartile range containing 50% of the data, with the median indicated by the line inside the box, and the whiskers representing the total data range. The red curve shows the average loop size. The loop density, as illustrated in Fig. 24b, increases up to 1 dpa. Curves 6a to 6c are the measurement from 3 nearby cells. As the loops begin to interact and transform into dislocation segments, the density decreases with increasing dose, suggesting loop coalescence. It is important to note that the density was calculated by dividing the number of loops by the foil thickness and the image area.

4 DISCUSSION

4.1 The role of pre-existing dislocation cell structures on defect formation

One of the key microstructural features distinguishing AM 316 SS from wrought 316 is its dislocation cell structure from the rapid solidification. This structure consists of columnar cells with diameters of approximately 500 nm and cell walls containing dense dislocations that are approximately 100 nm thick [5, 50, 51]. The as-printed dislocation cell walls are enriched with Cr, Mo, and marginally Si, and are decorated with $MnSiO_3$ particles averaging about 19 nm in size. The influence of this dislocation cell structure on the accumulation of irradiation damage in AM 316 SS is of particular interest.

The high dislocation density of the cell structure (10^{14} m^{-2}) is hypothesized to play a role similar to the dense dislocations in CW stainless steels. CW stainless steels, with dislocation densities typically ranging from 10^{15} to 10^{16} m^{-2}, generally exhibit reduced swelling compared to their wrought counterparts (10^{12} m^{-2}) under both neutron [15–22] and ion irradiation [3, 23–25]. However, in some cases, low to moderate levels of CW (5-10%) have been found to enhance swelling instead at high temperatures [52].

While dislocations tend to exhibit a biased preference for interstitials, the overall high density of

dislocations in CW materials act to reduce vacancy supersaturation through their sink strength and thereby suppress void nucleation and growth. The suppression of point defect concentrations extends the incubation period for swelling. The steady state swelling rate appears to be insensitive to the degree of CW [17]. The exact mechanism—whether it is the suppression of void nucleation or the suppression of void growth—remains unclear. For instance, some studies [19, 20] attribute lower swelling in CW 316 to reduced void density. Others suggest it is due to smaller void size [16, 17, 25], while yet others indicate both reduced density and size of voids are contributing factors [3, 15]. These discrepancies may result from differences in the production of transmutation helium [53] or variations in irradiation temperatures across experiments.

In contrast to the generally observed suppression of swelling in CW 316 SS, recent studies reveal that AM 316 SS exhibits higher swelling than its wrought or annealed counterparts in the same irradiation environment. For instance, Jiang et al. observed that stress-relieved (SR) AM 316L swells more than its hot isostatic pressing (HIP) and wrought counterparts at 500°C to 600°C [3] under 5 MeV Fe ion irradiation at about 9 x 10^{-4} dpa/s. Similarly, Bellefon et al. found that as-built AM 316L swells more than solution-annealed (SA) and fully-recrystallized counterparts at 500°C under 3.5 MeV Fe ion irradiation with a flux of about 3.4×10^{12} ions/cm^2/s [7].

Furthermore, swelling in our LPBF 316L and LPBF 316H (2-3%) at 600°C to 10 dpa noticeably exceeds previous ion irradiation experiments on regular 316 stainless steels. For example, Johnston et al. reported a swelling of 0.2% in an annealed Type 316 stainless steel irradiated with 5 MeV Ni ions at the swelling temperature of 625°C to about 40 dpa with a dose rate of about 2×10^{-2} dpa/s [24]. Hudson irradiated solution-treated Type 316 stainless steel at 600°C with 46.5 MeV Ni ions to 16 dpa with a dose rate of 1-3$\times10^{-3}$ dpa/s, and reported a swelling of about 0.6% [54]. Thus, as-built AM 316 appears to exhibit higher swelling than both conventional CW and annealed 316 stainless steels. Additionally, Jiang et al. demonstrated that the steady-state swelling rate is similar between SR and HIP AM 316 [3], suggesting that the dislocation cell structure in AM 316 enhances swelling by shortening the incubation period.

The unexpected enhancement of swelling in AM 316 can be explained by the relative importance of dislocations and cavity sinks, characterized by the Q-parameter, as initially proposed by Lee and Mansur [55] and later refined by Lin et al [56]. The updated Q-parameter is defined as:

$$Q = \frac{S_d + S_l + S_b}{S_v}$$

where S_d is the dislocation sink strength, S_l is dislocation loop sink strength, S_b is bubble sink strength,

which is zero in this study, and S_v is the void sink strength. When the sink strengths of dislocations and voids are comparable (Q $\sim$1), the partitioning of vacancies to voids and interstitials to dislocations is most effective, leading to maximum void nucleation and growth.

The dislocation densities of LPBF 316L and LPBF 316H irradiated at 600°C to 10 dpa were measured with TEM, and are 2.1×10^{14} m^{-2} and 1.9×10^{14} m^{-2}, respectively. Using the density and size of the void and loops at 10 dpa, the Q-values are calculated to be 1.3 and 2.2 for LPBF 316L and LPBF 316H, respectively. In contrast, CW 316 has a much higher initial dislocation density (an initial $Q \gg 1$), causing most defects to recombine at dislocations, while annealed 316 has a very low initial dislocation density (an initial $Q \ll 1$), allowing defects to recombine in the matrix or at voids. As dislocation loops nucleate and grow, developing a non-negligible biased sink strength in annealed 316, or as the dislocations in cold-worked material annihilate or relax under high temperatures and irradiation, the Q value can approach 1 when the radiation damage (dpa) is sufficiently high. As a result, as-built AM 316, with its intermediate dislocation density and starting with a Q value closer to unity, is more susceptible to swelling than both its CW and annealed counterparts. This observation aligns with findings that 5-10% CW 316 swells more than its solution-annealed (SA) and heavily CW counterparts at high temperatures [52].

Next, the heterogeneous void distribution is discussed. Voids were preferentially observed at pre-existing dislocation cell walls in both LPBF 316L and LPBF 316H irradiated at 600°C, as shown in Fig. 8. Similarly, Jiang et al. reported preferential void formation along cell walls in stress-relieved (SR) AM 316L irradiated at 600°C [3]. Interestingly, at lower temperatures of 500°C and 550°C, void denuded zones and suppressed zones were observed, respectively. Bellefon et al. also noted suppressed void growth at pre-existing cell boundaries in as-built AM 316L irradiated at 500°C [7]. These observations suggest that the dislocation cell structure in AM 316 enhances void formation at the cell structure at high temperatures but suppresses void formation at the cell structure as temperatures decrease.

The causes of the non-uniform void distribution will be discussed in the context of (1) elemental segregation, (2) non-uniform strain fields, and (3) the Q-parameter.

1. Elemental Segregation: The swelling behavior of austenitic stainless steels strongly depends on composition [4, 24, 57–62], particularly in terms of its effect on the incubation period [52]. Cr and Mo segregation at cell boundaries was observed before irradiation. Regarding the effect of Cr, Johnston et al. demonstrated that swelling in Fe-Ni-Cr alloys increases with higher Cr content [57, 63]. The influence of Mo content is more complex; Mo has been shown to enhance swelling within certain temperature and composition ranges while suppressing swelling under other conditions [52].

Besides Cr and Mo, cell walls are also enriched with Si, O, and Mn due to the distribution of $MnSiO_3$ particles. Oxygen stabilizes vacancy clusters by reducing the surface energy of voids and therefore can

enhance void formation in stainless steels [64–66]. The effects of Si and Mn are more complex; swelling increases with increasing Si content up to approximately 0.2 wt%, after which it decreases with further increases in Si content [52]. Conversely, swelling decreases with increasing Mn content up to about 1 wt%, then increases with further Mn enrichment [67]. The average concentrations of Si and Mn in LPBF 316L and LPBF 316H are 0.46/0.45 wt% and 1.19/1.09 wt%, respectively, both of which exceed their respective inversion concentrations. If ion mixing causes Si and Mn enrichment near $MnSiO_3$ particles, void swelling may be encouraged or discouraged along the cell walls, respectively. Bellefon et al. observed locally-enhanced void nucleation near $MnSiO_3$ particles at 500°C [7], but in our study at 600°C, preferential void nucleation near $MnSiO_3$ particles was not observed in either LPBF 316L or LPBF 316H.

Regarding Ni, although Ni was not initially segregated at dislocation cell walls, RIS at dislocations could lead to Ni enrichment at these sites. This aligns with the observed preferential Ni-rich precipitates in the LPBF 316H irradiated at 600°C, as shown in Fig. 10 and Fig. 11. Johnston et al. reported that swelling in austenitic stainless steels decreases with increasing Ni content up to 40 wt% [57]. Therefore potential Ni segregation at dislocation cell walls due to RIS can not account for the preferential void formation along these structures.

In summary, the preferential void swelling at cell boundaries aligns with the segregation of Cr, O, and Mn but is inconsistent with the behavior of Ni and Si. The effect of Mo segregation requires further investigation. Drawing a definitive conclusion about the role of segregation in heterogeneous void formation is challenging at this stage. The segregation at cell boundaries is only slightly concentrated; for instance, Cr is enriched by only 1–1.5 wt% compared to the matrix. Previous studies on the compositional effects on swelling in 316 stainless steels were based on much broader compositional ranges. It remains uncertain whether such minor enrichment can explain the observed heterogeneity in void distribution.

Additionally, inhomogeneous void distribution has been reported in solution-annealed and cold-worked 316 stainless steels [20, 65], indicating that elemental segregation is not a prerequisite for heterogeneous void formation. Finally, and perhaps most decisively, preferential void formation was observed at cell walls but not at grain boundaries, as shown in Figures 8, 10, and 11. Since the segregation levels at cell walls and grain boundaries are similar, this suggests that segregation, while can some effect, is not the primary factor driving heterogeneous void formation observed under the current irradiation condition.

2. The inhomogeneous strain field associated with dislocation cell structures is another potential cause for preferential void formation. Kohnert and Capolungo demonstrated that compressive and tensile strains from dislocations can accelerate and decelerate void growth, respectively [68]. However, several pieces of evidence suggest that the strain field is not a controlling factor for preferential void swelling at cell

boundaries.

First, the dislocation cell structure diminishes as early as 2 dpa in both LPBF 316L and LPBF 316H, as shown in Figures 4 and 5; meanwhile, voids are only observable after retro-projected onset doses of 3.5 dpa and 4.9 dpa, respectively. Second, since the relative strain between the cell wall and cell interior should be insensitive to irradiation temperature, the strain effect cannot explain the observations by Jiang et al. [3], where void enhancement at cell walls transitions to suppression as the temperature decreases from 600°C to 500°C. Lastly, previous studies have shown that in cold-worked metals, cell walls are under tensile strain while the interiors are under compressive strain [69–71]. A recent EBSD study also shows that cell walls are under tensile stresses while cell interiors are under compressive stresses [72]. This further indicates that the strain field nearby likely cannot account for the enhanced void swelling at cell walls during irradiation at 600°C.

3. The preferential void formation at cell walls may be understood using the Q-parameter. As discussed by Lee and Mansur [65], patchy voids are often observed during the early swelling stage in regions of relatively high dislocation density in wrought solution-annealed alloys and in regions of relatively low dislocation density in CW alloys. Preferential void nucleation occurs in areas where defects are partitioned nearly equally among biased and unbiased sinks (Q $\sim$1) is first fulfilled. In the case of LPBF 316L and LPBF 316H irradiated at 600°C, the cell walls, instead of cell interiors, exhibit a dislocation density that achieves a balanced sink strength between dislocations and cavities (Q $\sim$1). This balance lowers the critical cavity radius for nucleation, resulting in enhanced void formation. The absence of voids formation at grain boundary can also be explained accordingly; grain boundary is neutral sink, lacking dislocation bias and therefore having Q $\ll$ 1.

Nevertheless, the same question raised against the strain effect also applies to the Q-parameter: if the dislocation cell structure has mostly disappeared by 2 dpa, how can it still influence the void formation observed at much later doses? We hypothesize that void nuclei smaller than the resolving power of TEM have already formed at cell walls before 2 dpa. Further advanced characterization and modeling investigations will be needed to verify this hypothesis.

Regarding irradiation-induced dislocation loops, dislocation cell structures mainly affect the initial phase of loop formation in both LPBF 316L and 316H. By 600°C and 2 dpa, dislocation cell structures mostly disappeared, and large dislocation loops are randomly distributed, as *ex-situ* experiments revealed. Since large loops are absent at 0.2 dpa, the interaction between emerging dislocation loops and the dislocation cell structures wasn't captured by the *ex-situ* experiments. Conversely, *in-situ* experiments provided insight, demonstrating that dislocation loops first formed at the centers of dislocation cells and then extended toward the cell walls as the dose increases. This finding aligns with prior *in-situ* studies by

Li and Shang et al. [5, 6], which also indicated that dislocations at cell walls absorbed irradiation-induced dislocation loops, resulting in a reduced loop density in AM 316 compared to their wrought counterparts. However, previous neutron irradiation experiments have shown that there is insignificant differences in loop density between SA and CW stainless steels after irradiation at temperatures above 350°C to doses larger than 5 to 10 dpa [39]. In addition, our *ex-situ* observation indicates that the loop density at 300°C ($\sim 10^{22}$ m^{-3}) and 600°C ($\sim 10^{19}$ -10^{20} m^{-3}) at 10 dpa is in line with previous neutron irradiation data [39] and Fe ion irradiation data [73]. Therefore, once the dislocation cell structure is replaced by a dislocation network at high doses, the benefit of the dislocation cell structure for reducing dislocation loops diminishes.

Both *in-situ* and *ex-situ* observations of dislocation loop evolution at 600°C is consistent with the common observation in conventional stainless steels, in which the loop density reaches a maximum after a low dose and slightly decreases with further increases in dose [22, 39, 73, 74]. As shown in Fig. 24, the *in-situ* experiment indicates that the loop density peaks at 1 dpa. For the *ex-situ* irradiation (Fig. 14), the loop density declines after 2 dpa. Regarding dislocation loop size, *in-situ* experiments showed that loop growth slows after 3 dpa, while *ex-situ* experiments showed that the size began to decrease at 2 dpa. Similarly, for *ex-situ* irradiation at 300°C, the loop density peaks at 2 dpa and 5 dpa for LPBF 316H and LPBF 316L, respectively. These observations indicate that despite the pre-existing dislocation cell structure, loops can still develop within the dislocation-free interiors of these cells. The loop density rises quickly with increasing dose up to a peak, after which loops start to interact with pre-existing dislocation cells and with one another, forming a dislocation network that eventually reduces the number of dislocation loops, approaching a saturated value similar to conventional 316 stainless steels at high doses.

4.2 Carbon effect

The carbon effect on the microstructral evolution of LPBF 316L and LPBF 316H under irradiation is discussed with respect to four aspects: (1) $M_{23}C_6$ carbides, (2) void swelling, (3) dislocation loops and (4) irradiation hardening.

(1) $M_{23}C_6$ carbides are commonly observed in conventional stainless steels under high-temperature applications at $\sim$ 500°C to 900°C and contribute to a reduction in corrosion resistance of the steel by sensitization. In this study, at 600°C, $M_{23}C_6$ carbides were observed in LPBF 316H but not in LPBF 316L, after irradiation to a dose as low as 0.2 dpa, as shown in Fig. 20. The irradiation time for 0.2 dpa is 3.3 minutes. LPBF 316H annealed at 600°C for 1.5 hours showed no visible $M_{23}C_6$ carbides [50], indicating that irradiation significantly enhanced the rate of carbide precipitation. The absence of $M_{23}C_6$ in LPBF 316L can be understood with the lower driving force due to lower carbon concentration. On

the other hand, the absence carbides in LPBF 316H at 300°C is likely due to insufficient diffusion at this temperature, which is consistent with the TTT diagrams reported in Ref. [46, 75]

For LPBF 316H irradiated at 600°C, it is interesting to note that $M_{23}C_6$ carbides were only observed at grain boundaries, and not at the pre-existing dislocation cell walls (Fig. 11), even though a high dislocation density is anticipated to serve as a preferential nucleation site. This is understandable, first, since the cell structure has already vanished at least by 2 dpa. Second, there is no carbon segregation along cell walls in the first place to promote the nucleation of a carbide compositionally. Cr, on the other hand, is enriched at cell walls to begin with. Apparently, the Cr segregation is insufficient to promote $M_{23}C_6$ carbide formation at cell walls and requires the diffusion and accumulation of carbon while competing against cell wall dissolution. Finally, the carbon content in our LPBF 316H is only 0.04 wt%. It is likely that the precipitation of $M_{23}C_6$ at grain boundaries used up any free or excess carbon, leaving insufficient carbon in the matrix to nucleate carbides at other possible nucleation sites, such as dislocations. The later point is supported by the observation of carbide coarsening as shown in Fig. 20.

(2) As shown in Figures 8 and 9, the addition of carbon appears to delay the onset of void nucleation. Consistently, Williams reported that swelling decreased with increasing carbon level from 0.005 wt% to 0.03% in 316 stainless steels irradiated with Ni ions at 600°C [76]. It has also been suggested that carbon additions shift the peak swelling to higher temperatures [52, 77]. The carbon-vacancy binding affects the migration of vacancies [78–80]. The vacancy trapping by carbon was considered to be the underlying mechanism accounting for the carbon effect on the swelling rate and peak swelling temperature in 316 stainless steels [77]. Previously, a peak temperatures ~625-650°C was reported in solution-treated 316 stainless steel (0.03 wt%) irradiated with 46.5 MeV Ni ions with a damage rate of 1-3 $\times 10^{-3}$ dpa/s [54], and in annealed 316 stainless steel (0.055 wt% C) irradiated with 5 MeV Ni ions with a damage rate of 2×10^{-2} dpa/s. In our study, the additional carbon in LPBF 316H likely moved the peak swelling temperature further away from the irradiation temperature (600°C), resulting in lower swelling. Nevertheless, it should be noted that there are other causes that may also contribute to the swelling difference between LPBF 316L and LPBF 316H, such as the machine and powder variability. A single-variable effect study will be needed to confirm the carbon effect on void swelling in AM 316 stainless steels.

(3) Carbon content can also affect the formation of dislocation loops and therefore swelling through the dislocation bias. Williams showed that the mean loop size decreases with increasing carbon content (0.005 to 0.03 wt%) in 316 stainless steel irradiated with Ni ions at 500°C and 600°C to 1 dpa [76]. One possible effect of carbon on the loop evolution is its effect on stacking fault energy (SFE). The SFE generally increases with increasing carbon content in austenitic stainless steels [81, 82]. A higher SFE can lead to a smaller loop size; Hashimoto et al. showed that the average loop size decreases from 24.5 nm to

18.5 nm for $CoCrFeNiMn_x$ alloys with a SFE increasing from 21 mJ/m^2 to 36 mJ/m^2 [83]. In our study, based on the correlation developed by Brofman and Ansell [82], the SFE increment for a carbon content increasing from 0.006 wt% to 0.04 wt% is 0.9 mJ/m^2 [83], which is very small compared to the typical SFE of austenitic stainless steels of 20 mJ/m^2. Beside, the average loop size in LPBF 316H, which should have higher SFE, is larger than the average loop size in LPBF 316L for most of the dose/temperature combinations examined. Therefore, the carbon effect on SFE is unlikely a primary factor controlling the loop size in this study.

Nakata et al. showed that the loop density was insensitive to carbon content (0.005 wt% to 0.086 wt%) in 316 stainless steels irradiated with 1 MeV electrons at 400°C to 600°C to 0.5 dpa [84]. In our study, however, the effect of carbon on dislocation loop density is evident at 0.2 dpa. The loop density is higher in LPBF 316H versus LPBF 316L at both 300°C and 600°C. The comparison between ion and electron irradiation suggests an interplay of carbon with the displacement cascade. Nevertheless, with increasing dose, the trend became weaker and any effect due to carbon content is less obvious likely because of the complex interactions of dislocation network, voids, and $M_{23}C_6$ carbide formation, especially the latter, which decreases the carbon concentration in solution. In general, the current data of this study do not reveal a simple dependence of dislocation loop morphology on carbon content in LPBF 316 stainless steels. In addition, the observation is not consistent with the observation in regular 316 reported previously with high-energy electron irradiation. A more dedicated study focusing on the early stages of irradiation damage and dislocation loop formation, before the formation dislocation network and $M_{23}C_6$ carbides, is needed to understand the effect of carbon on dislocation loop evolution.

(4) Fig. 22(c-d) compares the nanohardness of LPBF 316L and LPBF 316H irradiated at 300ºC and 600°C. In general, the two materials exhibit similar hardening evolution. However, the initial hardness of the two materials should be discussed. The as-built LPBF 316H is 13% harder than LPBF 316L. This is consistent with the difference in microhardness measurement, 11%, as well as the difference in room temperature yield strength, 12% [10, 27]. The consistency between the hardness measurements and the tensile tests affirms the linear relationship between the two [85, 86]. While carbon is expected to enhance the strength through solution hardening, the differing carbon contents in these two specimens does not seem to fully account for the observed differences. For these LPBF 316L and LPBF 316H specimens, we calculate an increase in yield strength of —1564 MPa per weight percent of carbon, which is much higher than the 308 MPa/wt% C found for 15Cr-15Mn-4Ni austenitic stainless steel [87] and 347 stainless steel [88]. In addition, Sun et al. and Aoki et al. measured the Vickers hardness of 316 stainless steels as a function of carbon content [89, 90]. The data indicate that the hardness would increase from 207 HV to 212 HV for 316 stainless steels containing the same carbon concentration as LPBF 316L and LPBF

316H, respectively, leading to an increment 2.4%, which is also significantly smaller than the observed difference in this study.

Factors other than carbon concentration, such as powder's batch-to-batch variation, machine variation, and printing parameters, may also play a role. Zhang et al. tensile-tested LPBF 316 with carbon concentrations 0.04 wt% (the same material as this study), 0.053 wt%, and 0.07 wt%. All materials were printed in the same machine with the same printing parameter. These results indicated no obvious dependence of the tensile properties on the carbon content [91]. Conversely, appreciable differences in the mechanical properties were observed for AM 316 printed with the same powder but with different machines and even printed with the same machine but in different batches. As noted in Section 2, the LPBF 316L studied in this work was printed at ORNL with a Concept laser M2 system, while the LPBF 316H was printed at ANL with a Renishaw AM400 system. The microstructural differences resulting from the different printing process likely has a more pronounced effect on the observed initial hardness than the carbon concentration.

5 CONCLUSION

This study investigated the irradiation damage in as-built LPBF 316L and LPBF 316H stainless steels that were *ex-situ* irradiated with 4 MeV Ni^{2+} ions at 300°C and 600°C up to 10 dpa, and *in-situ* irradiated with 1 MeV Kr^{2+} ions at 600°C to 5 dpa. Overall, this study highlights the roles of initial AM microstructure on the interplay between irradiation conditions, material composition, and microstructural evolution. These insights are essential for the future development and deployment of LPBF stainless steels in reactor environments. The key findings are summarized below:

- Both materials initially exhibited a dislocation cell structure, which gradually diminished and evolved into a uniform dislocation structure by 2 dpa at both temperatures. At high doses, the dislocation structures in both materials converged to those typically observed in wrought stainless steels under comparable ion irradiation conditions.

- At 300°C, a high density of small defects, including SFT and dislocation loops, was produced by irradiation and quickly obscured the original dislocation cells. At 600°C, the dislocation cell walls broadened and reorganized, suggesting dislocation disentanglement facilitated by irradiation-induced defects. Meanwhile, new dislocation loops initially formed within the cell interiors and progressively extended toward the cell walls with increasing dose.

- At 300°C, voids were sparse at low doses, and not observed at high doses. At 600°C, however, faceted voids were observed in both materials at 5 dpa and 10 dpa, primarily along the initial

dislocation cell walls, albeit the dislocation cell structure had already been replaced by uniform dislocation structure at lower doses. While the exact micro-mechanism responsible for the unique development of voids in AM materials is not clear at present, it might be linked to the balanced sink strength between dislocation and cavities at cell walls, giving a Q-parameter closer to 1 as compared to the cell interior under the given irradiation condition.

- LPBF 316L exhibited a higher swelling percentage due to an earlier onset of void formation and a marginally higher swelling rate compared to LPBF 316H. As-built LPBF 316L and LPBF 316H appeared to have greater swelling than wrought or cold-worked 316 stainless steels irradiated under similar ion irradiation condition, potentially also due to a Q-value closer to 1.
- Irradiation-enhanced formation of $M_{23}C_6$ carbides were observed at grain boundaries in LPBF 316H irradiation at 600°C, but was absent at 300°C, nor in LPBF 316L irradiated at either temperatures. Carbides were not observed at dislocation cell boundaries.
- Ni-Si precipitates with a core-shell structure — Si cores and Ni shells — were predominantly observed along the original dislocation cell walls, coexisting with irradiation-induced voids. The heterogeneous distribution of Ni-Si precipitates manifests the enduring influence of initial microstructral heterogeneity of as-built LPBF 316 SS.
- The nanoindentation measurements showed the hardness evolution, indicating rapid hardening up to 2 dpa at 300°C, followed by softening, and at 600°C, softening at low doses was followed by hardening, which is qualitatively in line with the microstructure observation.
- Combining the observations in dislocation structures, voids, precipitation and hardness measurement, it appears that at 300°C the defect structure stabilized between 2 to 5 dpa. At 600°C, while dislocation structures somewhat stabilized after 2 dpa, precipitation, void formation, and hardening continued to evolve.

ACKNOWLEDGMENTS

This work was sponsored by the U.S. Department of Energy, Office of Nuclear Energy, Advanced Materials and Manufacturing Technologies (AMMT) program, under Contract No. DE-AC02-06CH11357 with Argonne National Laboratory, managed and operated by UChicago Argonne LLC, by UT-Battelle, LLC, under contract DE-AC05-00OR22725, and Battelle Energy Alliance LLC under contract DE-AC07-05ID14517. Dr. Thak Sang Byun and Dr. Caleb Massey from Oak Ridge National Laboratory are thanked for providing the materials used for this study. Dr. Robert Erck is thanked for providing the access of optical profilometer. Dr. Hi Vo and Dr. Matt Schneider were thanked for the advice in performing

nanoindentation. Dr. Yuzi Liu was thanked for providing assistance in focused ion beam. Dr. Jianguo Wen and Mr. Hanyu Hou were thanked for EELS measurement. The Work performed at the Center for Nanoscale Materials, a U.S. Department of Energy Office of Science User Facility, was supported by the U.S. DOE, Office of Basic Energy Sciences, under Contract No. DE-AC02-06CH11357.

REFERENCES

[1] Stephen Taller et al. “An approach to combine neutron and ion irradiation data to accelerate material qualification for nuclear reactors”. In: *Journal of Nuclear Materials* (2024), p. 155385.

[2] Andrea M Jokisaari et al. “Promoting regulatory acceptance of combined ion and neutron irradiation testing of nuclear reactor materials: Modeling and software considerations”. In: *Progress in Nuclear Energy* 178 (2025), p. 105518.

[3] Li Jiang et al. “A comparison study of void swelling in additively manufactured and cold-worked 316L stainless steels under ion irradiation”. In: *Journal of Nuclear Materials* 551 (2021), p. 152946.

[4] Miao Song et al. “Void Swelling in Additively Manufactured 316L Stainless Steel with Hafnium Composition Gradient under Self-Ion Irradiation”. In: *Journal of Nuclear Materials* 578 (May 2023), p. 154351. ISSN: 0022-3115. DOI: 10.1016/j.jnucmat.2023.154351. (Visited on 12/11/2024).

[5] Z Shang et al. “Response of solidification cellular structures in additively manufactured 316 stainless steel to heavy ion irradiation: an in situ study”. In: *Materials Research Letters* 7.7 (2019), pp. 290–297.

[6] Shilei Li et al. “Evolution of cellular dislocation structures and defects in additively manufactured austenitic stainless steel under ion irradiation”. In: *Scripta Materialia* 178 (2020), pp. 245–250.

[7] G Meric De Bellefon et al. “Influence of solidification structures on radiation-induced swelling in an additively-manufactured austenitic stainless steel”. In: *Journal of Nuclear Materials* 523 (2019), pp. 291–298.

[8] M McMurtrey et al. “Investigation of the irradiation effects in additively manufactured 316L steel resulting in decreased irradiation assisted stress corrosion cracking susceptibility”. In: *Journal of Nuclear Materials* 545 (2021), p. 152739.

[9] Marie Loyer-Prost et al. “Impact of intragranular misorientation on void swelling and inter-granular cavities after ion irradiation in standard and additive manufacturing 316L austenitic steels”. In: *Journal of Nuclear Materials* 573 (2023), p. 154102.

[10] TS Byun et al. “Mechanical behavior of additively manufactured and wrought 316L stainless steels before and after neutron irradiation”. In: *Journal of Nuclear Materials* 548 (2021), p. 152849. ISSN: 0022-3115.

[11] Zhongxia Shang et al. “Heavy ion irradiation response of an additively manufactured 316LN stainless steel”. In: *Journal of Nuclear Materials* 546 (2021), p. 152745.

[12] Y Morris Wang et al. “Additively manufactured hierarchical stainless steels with high strength and ductility”. In: *Nature materials* 17.1 (2018), pp. 63–71.

[13] Yuan Zhong et al. “Intragranular cellular segregation network structure strengthening 316L stainless steel prepared by selective laser melting”. In: *Journal of Nuclear Materials* 470 (2016), pp. 170–178.

[14] Leifeng Liu et al. “Dislocation network in additive manufactured steel breaks strength–ductility trade-off”. In: *Materials Today* 21.4 (2018), pp. 354–361.

[15] HR Brager. “The effects of cold working and pre-irradiation heat treatment on void formation in neutron-irradiated type 316 stainless steel”. In: *Journal of Nuclear Materials* 57.1 (1975), pp. 103–118.

[16] JI Bramman et al. *VOID FORMATION IN CLADDING AND STRUCTURAL MATERIALS IRRADIATED IN DFR.* Tech. rep. United Kingdom Atomic Energy Authority, Dounreay (Scotland). Reactor Group, 1972.

[17] S Hamada et al. “Temperature dependence of swelling in type 316 stainless steel irradiated in HFIR”. In: *Journal of Nuclear Materials* 155 (1988), pp. 838–844.

[18] Janez Megusar. “Swelling Resistance of the Highly Deformed Titanium-Modified Austenitic Stainless Steel”. In: *Effects of Radiation on Materials: 14th International Symposium (Volume I)*. ASTM International. 1990.

[19] JL Straalsund and HR Brager. *EFFECTS OF COLD WORK ON VOID FORMATION IN AUSTENITIC STAINLESS STEEL.* Tech. rep. Hanford Engineering Development Lab., Richland, WA (United States), 1971.

[20] JF Stubbins et al. “Microstructural Evolution of Neutron Irradiated Fe-Cr-Ni Alloys at 495° C in Response to Changes in the Helium/DPA Ratio”. In: *Effects of Radiation on Materials: 14th International Symposium (Volume I)*. ASTM International. 1990.

[21] Masahide Suzuki et al. “Microstructural development of titanium-modified austenitic stainless steel under neutron irradiation in HFIR up to 57 dpa”. In: *Effects of Radiation on Materials: 14th International Symposium (Volume I)*. ASTM International. 1990.

[22] Shozo Hamada et al. “The Microstructural Evolution and Swelling Behavior of Type 316 Stainless Steel Irradiated in HFIR”. In: *Effects of Radiation on Materials: 14th International Symposium (Volume I)*. ASTM International. 1990.

[23] RS Nelson et al. *VOID FORMATION IN METALS DURING ION BOMBARDMENT.* Tech. rep. Atomic Energy Research Establishment, Harwell (England), 1972.

[24] WG Johnston et al. “Nickel-ion bombardment of annealed and cold-worked type 316 stainless steel”. In: *Journal of nuclear materials* 48.3 (1973), pp. 330–338.

[25] DW Keefer and AG Pard. “Void Formation in Cold-Worked Type 316 Stainless Steel Irradiated with 1-MeV Protons”. In: *Properties of Reactor Structural Alloys After Neutron or Particle Irradiation*. ASTM International, 1975.

[26] ASTM International. *Standard Specification for Chromium and Chromium-Nickel Stainless Steel Plate, Sheet, and Strip for Pressure Vessels and for General Applications, ASTM A240/A240M-16a*. Standard. 2016.

[27] Xuan Zhang et al. *Development of process parameters and post-build conditions for qualification of LPBF 316 SS. ANL-AMMT-004*. Report. Argonne National Laboratory (ANL), Argonne, IL (United States), 2023.

[28] Xuan Zhang et al. “In situ high-energy X-ray study of deformation mechanisms in additively manufactured 316L stainless steel”. In: *Journal of Nuclear Materials* 549 (2021), p. 152874.

[29] Lin Gao, Srinivas Aditya Mantri, and Xuan Zhang. “Quantification of solution annealing effects on microstructure and property in a laser powder bed fusion 316H stainless steel”. In: *Materials & Design* (2025), p. 113692.

[30] T Ungár and A Borbély. “The effect of dislocation contrast on x-ray line broadening: A new approach to line profile analysis”. In: *Applied Physics Letters* 69.21 (1996), pp. 3173–3175.

[31] James F Ziegler, Matthias D Ziegler, and Jochen P Biersack. “SRIM–The stopping and range of ions in matter (2010)”. In: *Nuclear Instruments and Methods in Physics Research Section B: Beam Interactions with Materials and Atoms* 268.11-12 (2010), pp. 1818–1823. ISSN: 0168-583X.

[32] Meimei Li, Wei-Ying Chen, and Peter M Baldo. “In situ transmission electron microscopy with dual ion beam irradiation and implantation”. In: *Materials Characterization* 173 (2021), p. 110905. ISSN: 1044-5803.

[33] Pengcheng Zhu et al. “Toward accurate evaluation of bulk hardness from nanoindentation testing at low indent depths”. In: *Materials & Design* 213 (2022), p. 110317.

[34] William D Nix and Huajian Gao. “Indentation size effects in crystalline materials: a law for strain gradient plasticity”. In: *Journal of the Mechanics and Physics of Solids* 46.3 (1998), pp. 411–425.

[35] Fuyao Yan et al. “Characterization of nano-scale oxides in austenitic stainless steel processed by powder bed fusion”. In: *Scripta Materialia* 155 (2018), pp. 104–108.

[36] Thak Sang Byun et al. *Mechanical properties and Deformation Behavior of Additively Manufactured 316L Stainless Steel (FY2020)*. Tech. rep. Oak Ridge National Laboratory (ORNL), Oak Ridge, TN (United States), 2020.

[37] Dan Mordehai and Georges Martin. “Enhanced annealing of the dislocation network under irradiation”. In: *Physical Review B—Condensed Matter and Materials Physics* 84.1 (2011), p. 014115.

[38] Frank A Garner. “Radiation-induced damage in austenitic structural steels used in nuclear reactors”. In: (2020).

[39] SJ Zinkle, PJ Maziasz, and RE Stoller. “Dose dependence of the microstructural evolution in neutron-irradiated austenitic stainless steel”. In: *Journal of Nuclear materials* 206.2-3 (1993), pp. 266–286.

[40] C Dimitrov et al. “Point Defects in FCC Fe-Cr-Ni Alloys”. In: *Materials Science Forum*. Vol. 15. Trans Tech Publ. 1987, pp. 1275–1280.

[41] Nghi Q Lam. “Radiation-induced defect buildup and radiation-enhanced diffusion in a foil under energetic bombardment”. In: *Journal of Nuclear Materials* 56.2 (1975), pp. 125–135.

[42] PJ Maziasz. “Overview of microstructural evolution in neutron-irradiated austenitic stainless steels”. In: *Journal of nuclear materials* 205 (1993), pp. 118–145.

[43] PJ Maziasz. “Formation and stability of radiation-induced phases in neutron-irradiated austenitic and ferritic steels”. In: *Journal of Nuclear Materials* 169 (1989), pp. 95–115.

[44] Miao Song et al. “Radiation damage and irradiation-assisted stress corrosion cracking of additively manufactured 316L stainless steels”. In: *Journal of Nuclear Materials* 513 (2019), pp. 33–44.

[45] Jingfan Yang et al. “Dislocation channel broadening–A new mechanism to improve irradiation-assisted stress corrosion cracking resistance of additively manufactured 316 L stainless steel”. In: *Acta Materialia* 266 (2024), p. 119650.

[46] B Weiss and R Stickler. “Phase instabilities during high temperature exposure of 316 austenitic stainless steel”. In: *Metallurgical and Materials Transactions B* 3 (1972), pp. 851–866.

[47] Thomas Sourmail. “Precipitation in creep resistant austenitic stainless steels”. In: *Materials science and technology* 17.1 (2001), pp. 1–14.

[48] Meimei Li et al. “Study of defect evolution by TEM with in situ ion irradiation and coordinated modeling”. In: *Philosophical Magazine* 92.16 (2012), pp. 2048–2078.

[49] Wei-Ying Chen et al. “Irradiation effects on Al0. 3CoCrFeNi and CoCrMnFeNi high-entropy alloys, and 316H stainless steel at 500° C”. In: *Journal of Nuclear Materials* 539 (2020), p. 152324.

[50] Wei-Ying Chen et al. *In-situ and ex-situ characterization of ion-irradiated AM materials*. Report. Argonne National Laboratory (ANL), Argonne, IL (United States), 2023.

[51] Wei-Ying Chen et al. *In-situ and ex-situ characterization of irradiated AM materials*. Tech. rep. Argonne National Laboratory (ANL), Argonne, IL (United States), 2024.

[52] Frank Garner. “Irradiation Performance of Cladding and Structural Steels in Liquid Metal Reactors”. In: *Materials Science and Technology*. John Wiley & Sons, Ltd, 2006. ISBN: 978-3-527-60397-8. DOI: 10.1002/9783527603978.mst0110. (Visited on 12/13/2024).

[53] N. H. Packan, K. Farrell, and J. O. Stiegler. “Correlation of Neutron and Heavy-Ion Damage: I. The Influence of Dose Rate and Injected Helium on Swelling in Pure Nickel”. In: *Journal of Nuclear Materials* 78.1 (Nov. 1978), pp. 143–155. ISSN: 0022-3115. DOI: 10.1016/0022-3115(78)90513-5. (Visited on 12/17/2024).

[54] JA Hudson. “Void formation in solution-treated aisi 316 and 321 stainless steels under 46.5 mev ni6+ irradiation”. In: *Journal of Nuclear Materials* 60.1 (1976), pp. 89–106.

[55] EH Lee and LK Mansur. “Unified theoretical analysis of experimental swelling data for irradiated austenitic and ferritic/martensitic alloys”. In: *Metallurgical Transactions A* 21 (1990), pp. 1021–1035.

[56] Yan-Ru Lin, Arunodaya Bhattacharya, and Steven J Zinkle. “The effect of helium on cavity swelling in dual-ion irradiated Fe and Fe-10Cr ferritic alloys”. In: *Journal of Nuclear Materials* 569 (2022), p. 153907.

[57] WG Johnston et al. “An experimental survey of swelling in commercial Fe-Cr-Ni alloys bombarded with 5 MeV Ni Ions”. In: *Journal of Nuclear Materials* 54.1 (1974), pp. 24–40.

[58] M. Suzuki et al. “Microstructural Development of Titanium-Modified Austenitic Stainless Steel Under Neutron Irradiation in HFIR up to 57 Dpa”. In: *Effects of Radiation on Materials: 14th International Symposium (Volume I)*. ASTM International, Jan. 1990. DOI: 10.1520/STP24638S. (Visited on 12/12/2024).

[59] Takahiko Kato, Heishichiro Takahashi, and Masakiyo Izumiya. “Effects of systematic modification with oversized elements on void formation in 316L austenitic stainless steel under electron irradiation”. In: *Materials Transactions, JIM* 32.10 (1991), pp. 921–930.

[60] FA Garner and HR Brager. “The influence of Mo, Si, P, C, Ti, Cr, Zr and various trace elements on the neutron-induced swelling of AISI 316 stainless steel”. In: *Journal of Nuclear Materials* 155 (1988), pp. 833–837.

[61] Jian Gan et al. “The effect of oversized solute additions on the microstructure of 316SS irradiated with 5 MeV Ni++ ions or 3.2 MeV protons”. In: *Journal of nuclear materials* 325.2-3 (2004), pp. 94–106.

[62] K Herschbach, W Schneider, and K Ehrlich. “Effects of minor alloying elements upon swelling and in-pile creep in model plain Fe-15Cr-15Ni stainless steels and in commercial DIN 1.4970 alloys”. In: *Journal of nuclear materials* 203.3 (1993), pp. 233–248.

[63] JF Bates and WG Johnston. “Effects of alloy composition on void swelling”. In: *Radiation effects in breeder reactor structural materials*. Metallurgical Society of AIME, 1977.

[64] SJ Zinkle and EH Lee. “Effect of oxygen on vacancy cluster morphology in metals”. In: *Metallurgical Transactions A* 21 (1990), pp. 1037–1051.

[65] EH Lee and LK Mansur. “Relationships between phase stability and void swelling in Fe-Cr-Ni alloys during irradiation”. In: *Metallurgical Transactions A* 23 (1992), pp. 1977–1986.

[66] LE Seitzman et al. “The effect of oxygen on void stability in nickel and austenitic steel”. In: *Journal of Nuclear Materials* 141 (1986), pp. 738–742.

[67] JF Bates, FA Garner, and FM Mann. “The effect of solid transmutation products on swelling in 316 stainless steel”. In: *Journal of Nuclear Materials* 104 (1981), pp. 999–1003.

[68] Aaron A Kohnert and Laurent Capolungo. “A Novel Approach to Quantifying the Kinetics of Point Defect Absorption at Dislocations”. In: *Journal of the Mechanics and Physics of Solids* 122 (2019), pp. 98–115.

[69] H. Mughrabi. “Dislocation Wall and Cell Structures and Long-Range Internal Stresses in Deformed Metal Crystals”. In: *Acta Metallurgica* 31.9 (Sept. 1983), pp. 1367–1379. ISSN: 0001-6160. DOI: 10.1016/0001-6160(83)90007-X. (Visited on 12/28/2024).

[70] T. Ungar et al. “X-Ray Line-Broadening Study of the Dislocation Cell Structure in Deformed [001]-Orientated Copper Single Crystals”. In: *Acta Metallurgica* 32.3 (Mar. 1984), pp. 333–342. ISSN: 0001-6160. DOI: 10.1016/0001-6160(84)90106-8. (Visited on 12/28/2024).

[71] E. M. Viatkina, W. A. M. Brekelmans, and M. G. D. Geers. “Modelling of the Internal Stress in Dislocation Cell Structures”. In: *European Journal of Mechanics - A/Solids* 26.6 (Nov. 2007), pp. 982–998. ISSN: 0997-7538. DOI: 10.1016/j.euromechsol.2007.05.001. (Visited on 12/28/2024).

[72] Sravya Tekumalla, Matteo Seita, and Stefan Zaefferer. “Delineating Dislocation Structures and Residual Stresses in Additively Manufactured Alloys”. In: *Acta Materialia* 262 (Jan. 2024), p. 119413. ISSN: 1359-6454. DOI: 10.1016/j.actamat.2023.119413. (Visited on 01/09/2025).

[73] Auriane Etienne et al. “Dislocation loop evolution under ion irradiation in austenitic stainless steels”. In: *Journal of nuclear materials* 400.1 (2010), pp. 56–63.

[74] H. R. Brager et al. *Stress-Affected Microstructural Development and Creep-Swelling Interrelationship*. Tech. rep. HEDL-SA-1167; CONF-770641-12. Hanford Engineering Development Lab., Richland, WA (United States), May 1977. (Visited on 01/02/2025).

[75] PJ Maziasz and CJ McHargue. “Microstructural evolution in annealed austenitic steels during neutron irradiation”. In: *International materials reviews* 32.1 (1987), pp. 190–219.

[76] TM Williams. “The effect of soluble carbon on void swelling and low dose dislocation structures in type 316 austenitic stainless steel irradiated with 46.5 MeV Ni6+ ions”. In: *Journal of Nuclear Materials* 88.2-3 (1980), pp. 217–225.

[77] MJ Makin, GP Walters, and AJE Foreman. “The void swelling behaviour of electron irradiated type 316 austenitic steel”. In: *Journal of Nuclear Materials* 95.1-2 (1980), pp. 155–170.

[78] S Takaki et al. “The resistivity recovery of high purity and carbon doped iron following low temperature electron irradiation”. In: *Radiation effects* 79.1-4 (1983), pp. 87–122.

[79] MP Short et al. “Modeling injected interstitial effects on void swelling in self-ion irradiation experiments”. In: *Journal of Nuclear Materials* 471 (2016), pp. 200–207.

[80] Chu Chun Fu et al. “Effect of C on vacancy migration in α-iron”. In: *Solid State Phenomena* 139 (2008), pp. 157–164.

[81] RE Schramm and RP Reed. “Stacking fault energies of seven commercial austenitic stainless steels”. In: *Metallurgical transactions A* 6 (1975), pp. 1345–1351.

[82] PJ Brofman and GS Ansell. “On the effect of carbon on the stacking fault energy of austenitic stainless steels”. In: *Metallurgical Transactions A* 9 (1978), pp. 879–880.

[83] N Hashimoto et al. “Effect of stacking fault energy on damage microstructure in ion-irradiated CoCrFeNiMnx concentrated solid solution alloys”. In: *Journal of Nuclear Materials* 545 (2021), p. 152642.

[84] Kiyotomo Nakata et al. “Effects of nitrogen and carbon on void swelling in electron-irradiated austenitic stainless steel”. In: *Journal of Nuclear Materials* 122.1-3 (1984), pp. 639–643.

[85] Jeremy T Busby, Mark C Hash, and Gary S Was. “The relationship between hardness and yield stress in irradiated austenitic and ferritic steels”. In: *Journal of Nuclear Materials* 336.2-3 (2005), pp. 267–278.

[86] EJ Pavlina and CJ Van Tyne. “Correlation of yield strength and tensile strength with hardness for steels”. In: *Journal of materials engineering and performance* 17 (2008), pp. 888–893.

[87] Nithi Saenarjhan, Jee-Hyun Kang, and Sung-Joon Kim. “Effects of carbon and nitrogen on austenite stability and tensile deformation behavior of 15Cr-15Mn-4Ni based austenitic stainless steels”. In: *Materials Science and Engineering: A* 742 (2019), pp. 608–616.

[88] One Yoo et al. “The effect of the carbon and nitrogen contents on the fracture toughness of Type 347 austenitic stainless steels”. In: *Materials Science and Engineering: A* 405.1-2 (2005), pp. 147–157.

[89] K Aoki et al. “Low temperature gas carburising for austenitic stainless steels: the NV-Pionite process”. In: *Stainless Steel 2000*. CRC Press, 2020, pp. 389–405.

[90] Y Sun, X Li, and T Bell. “Low temperature plasma carburising of austenitic stainless steels for improved wear and corrosion resistance”. In: *Surface Engineering* 15.1 (1999), pp. 49–54.

[91] Xuan Zhang, Lin Gao, and Srinivas Aditya Mantri. *Technical basis for understanding the process-microstructure-property correlation in LPBF 316 SS*. Tech. rep. Argonne National Laboratory (ANL), Argonne, IL (United States), 2024.

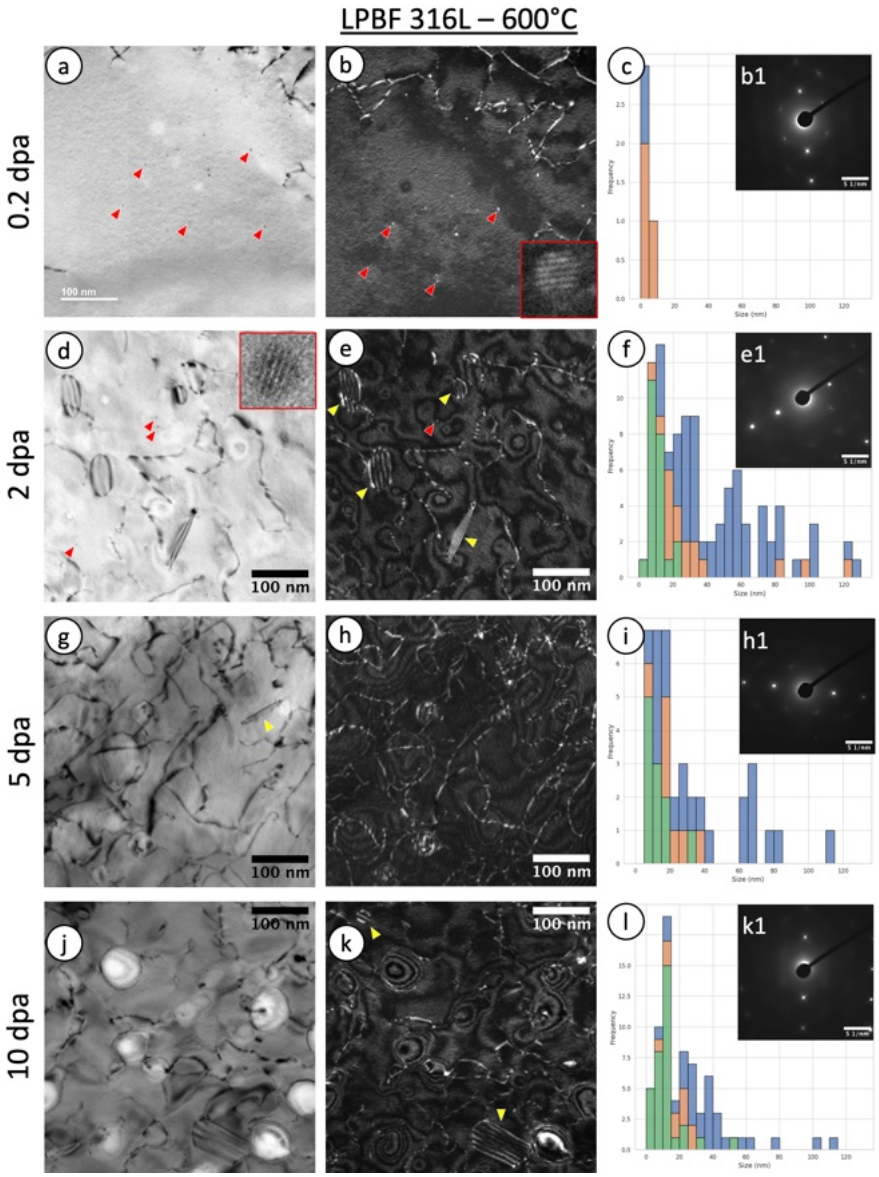

Figure 12. The BF and DF TEM images, diffraction patterns and the size distribution of dislocation loops of LPBF 316L *ex-situ* irradiated with 4 MeV Ni^{2+} ions at 600°C to (a-c) 0.2 dpa, (d-f) 2 dpa, (g-i) 5 dpa and (j-l) 10 dpa. The red arrows indicate the small precipitates. The yellow arrows indicate the faulted dislocation loops. The blue, orange and green colors in the size distribution correspond to the faulted, perfect and undetermined loops, respectively. The inset images show the magnified images of the small precipitates in the corresponding samples.

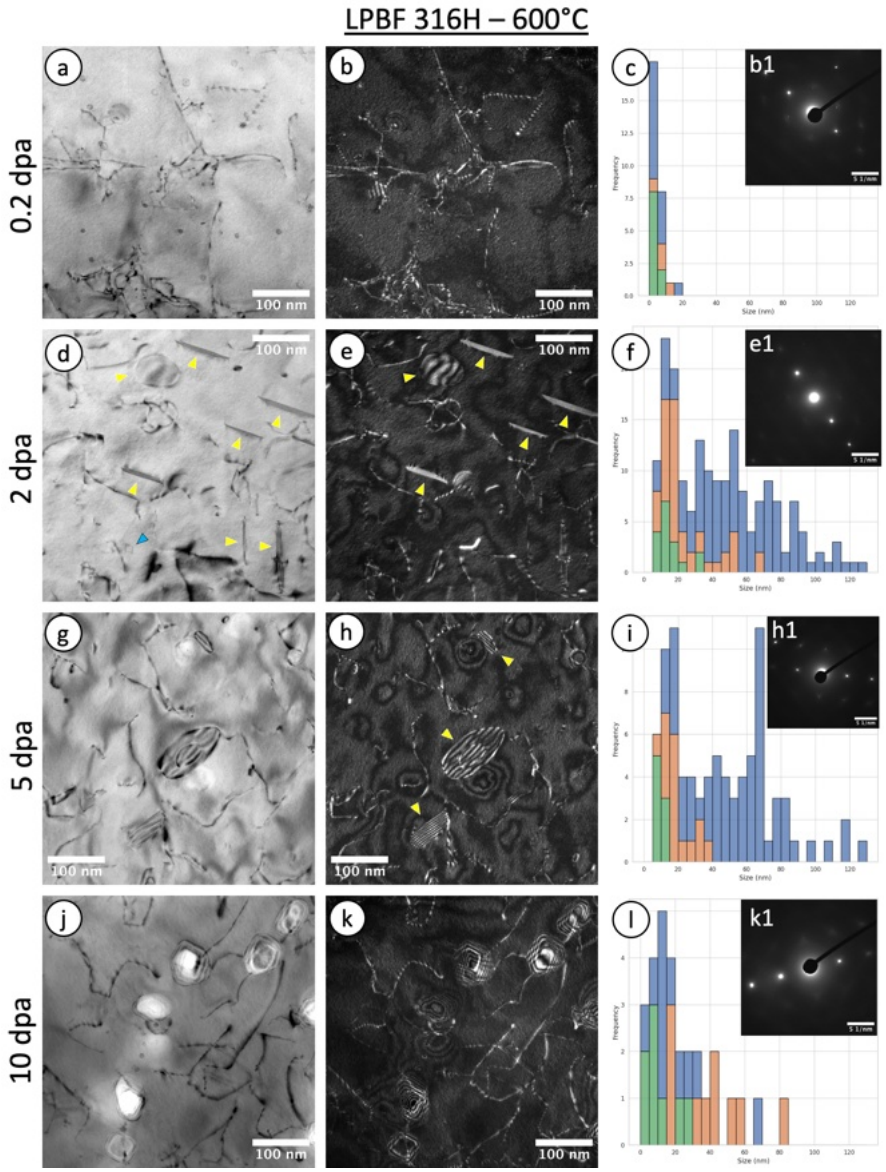

Figure 13. The BF and DF TEM images, diffraction patterns and the size distribution of dislocation loops of LPBF 316H *ex-situ* irradiated with 4 MeV Ni^{2+} ions at 600°C to (a-c) 0.2 dpa, (d-f) 2 dpa, (g-i) 5 dpa and (j-l) 10 dpa. The yellow arrows indicate the faulted dislocation loops. The blue arrow indicates a perfect dislocation loop. The blue, orange and green colors in the size distribution correspond to the faulted, perfect and undetermined loops, respectively.

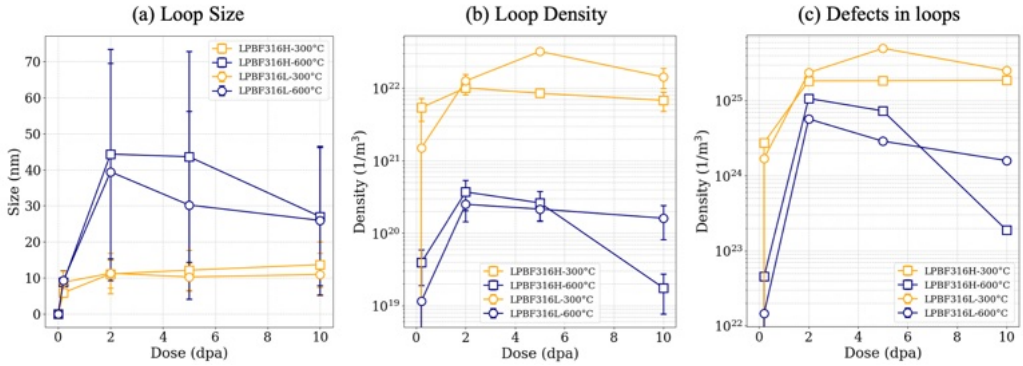

Figure 14. (a) Average loop size, (b) loop density (c) the amount of defects in dislocation loops larger than 5 nm in LPBF 316L and LPBF 316H *ex-situ* irradiated with 4 MeV Ni^{2+} ions at 300°C and 600°C as a function of dose.

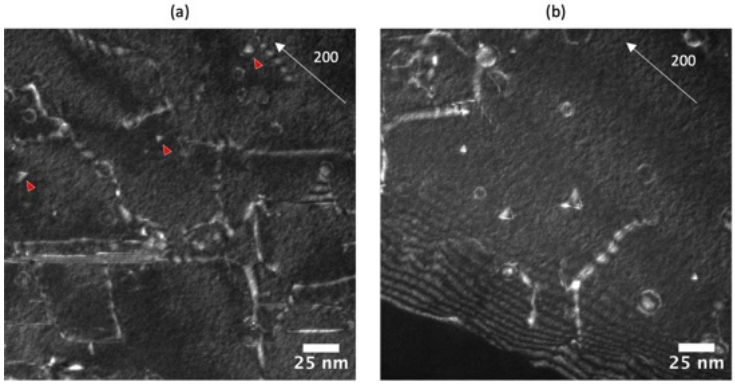

Figure 15. SFT observed in LPBF 316H *ex-situ* irradiated with 4 MeV Ni^{2+} ions at 600°C to 0.2 dpa where (a) is far from the grain boundary and (b) is near the grain boundary.

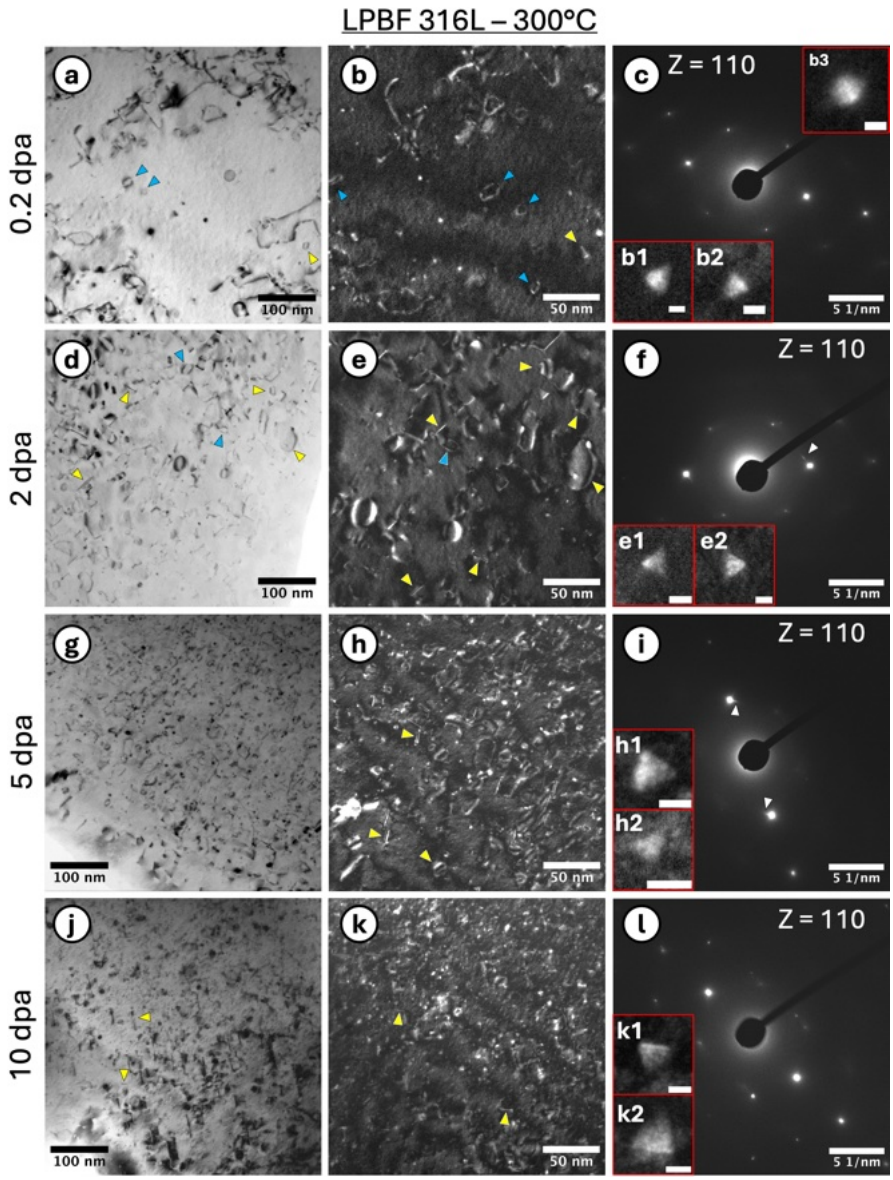

Figure 16. The (a, d, g, j) BF, (b, e, h, k) DF TEM images and (c, f, i, l) diffraction patterns of LPBF 316L *ex-situ* irradiated with 4 MeV Ni^{2+} at 300°C to (a-c) 0.2 dpa, (d-f) 2 dpa, (g-i) 5 dpa and (j-l) 10 dpa. The yellow arrows highlight the faulted loops. The blue arrows highlight perfect loops. The white arrows highlight the rel-rod streaks. The inset b1, b2 to k1, k2 are the SFT, and b3 is black spot defect found in the corresponding DF images where the scale bar is 3 nm.

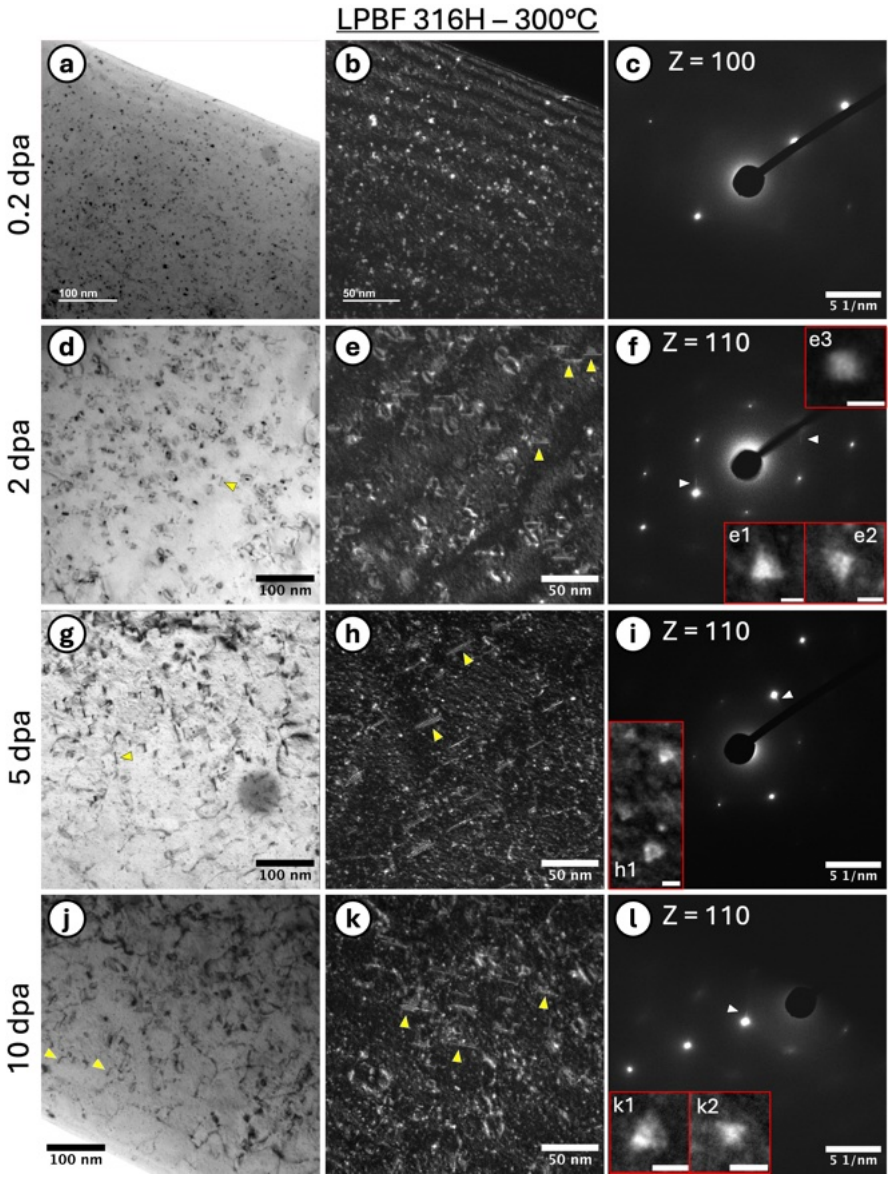

Figure 17. The (a, d, g, j) BF, (b, e, h, k) DF TEM images and (c, f, i, l) diffraction patterns of LPBF 316H irradiated with 4 MeV Ni^{2+} ions at 300°C to (a-c) 0.2 dpa, (d-f) 2 dpa, (g-i) 5 dpa and (j-l) 10 dpa. The inset e1, e2 to k1, k2 are the SFT, and e3 is the black spot defect found in the corresponding DF images where the scale bar is 3 nm.

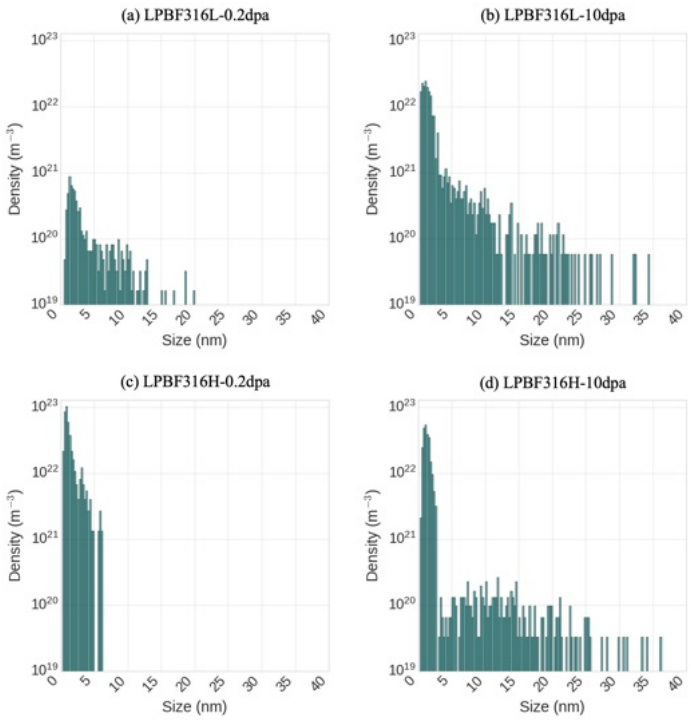

Figure 18. The defect size distribution of LPBF 316L and LPBF 316H irradiated at 300°C to (a) 0.2 dpa and (b) 10 dpa for LPBF 316L. (c) 0.2 dpa and (d) 2dpa for LPBF 316H. The bin size is 0.25 nm.

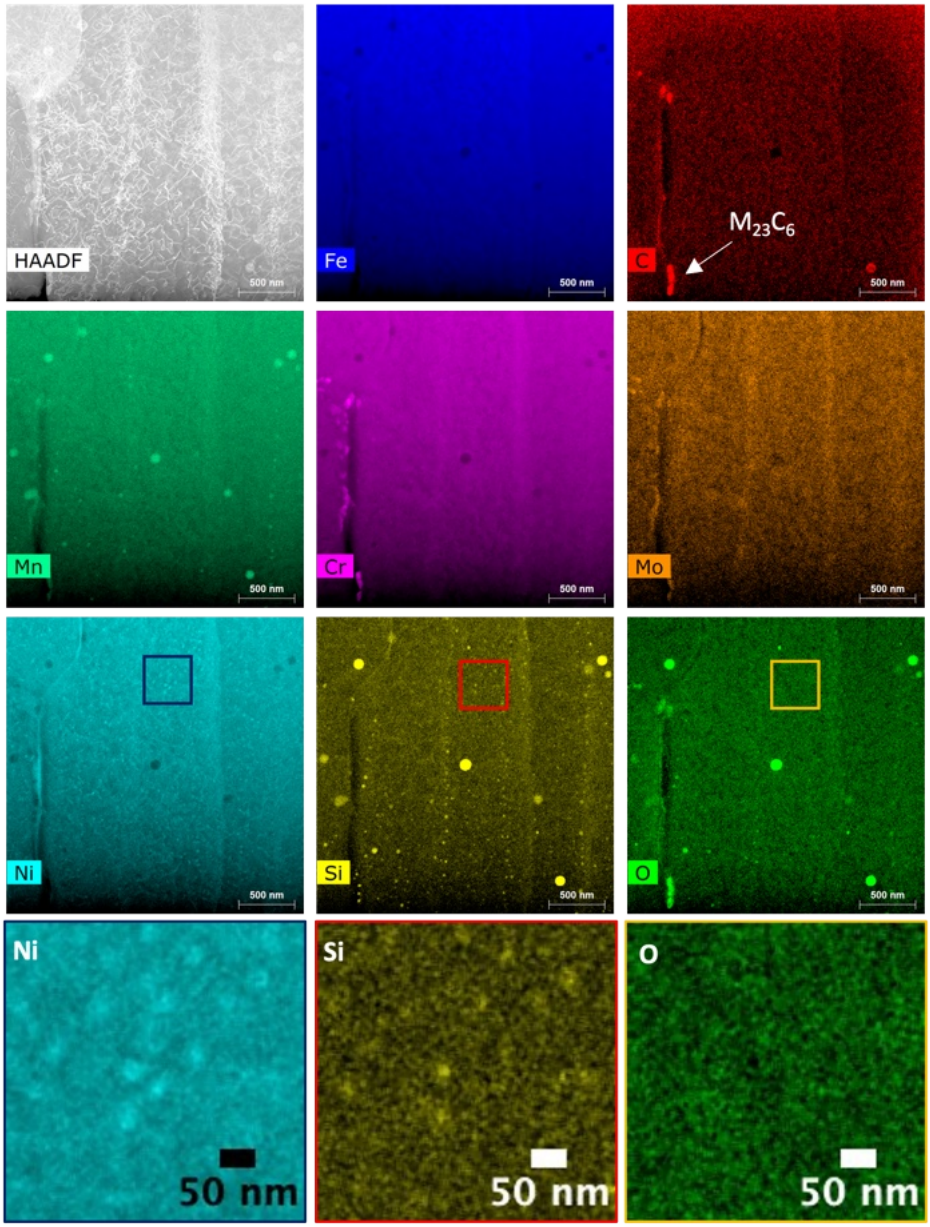

Figure 19. EDS intensity maps of LPBF 316H *ex-situ* irradiated with 4 MeV Ni^{2+} ions at 600°C to 2 dpa. The bottom row are magnified maps for Ni, Si and O.

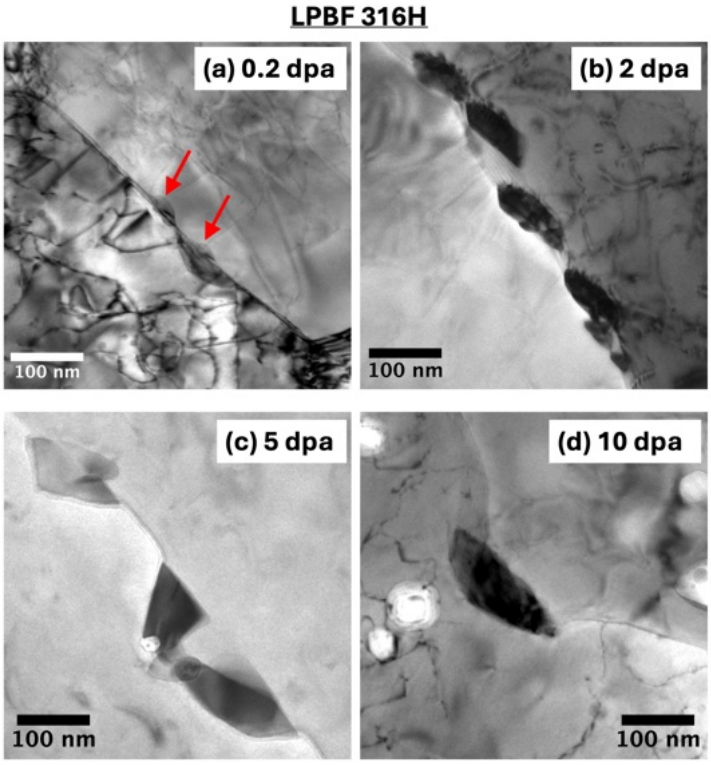

Figure 20. BF images of LPBF 316H *ex-situ* irradiated with 4 MeV Ni^{2+} ions at 600°C to (a) 0.2 dpa, (b) 2 dpa, (c) 5 dpa and (10) dpa, showing carbides forming at the grain boundaries.

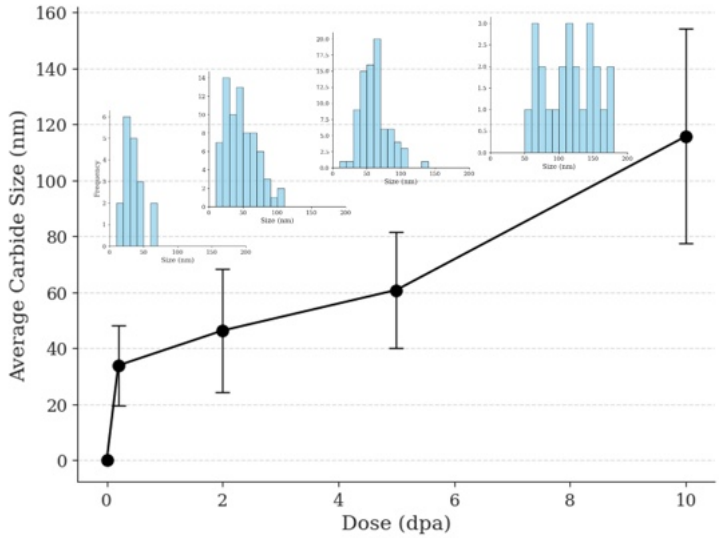

Figure 21. The size of $M_{23}C_6$ carbides observed at the grain boundary of LPBF 316H *ex-situ* irradiated with 4 MeV Ni^{2+} ions at 600°C as a function of dose. The error bar is the standard deviation.

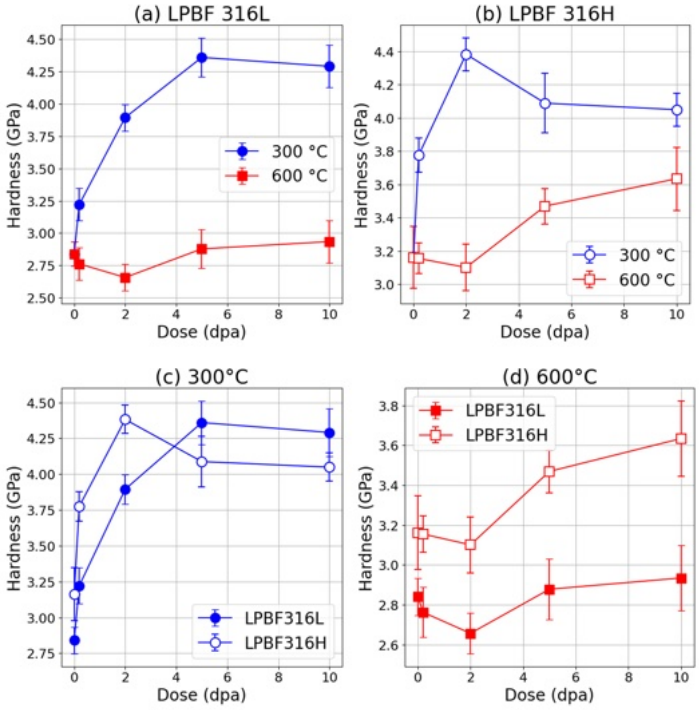

Figure 22. Nanohardness measured by nanoindentation on LPBF 316L and LPBF 316H *ex-situ* irradiated with 4 MeV Ni^{2+} ions as a function of temperatures and dose.

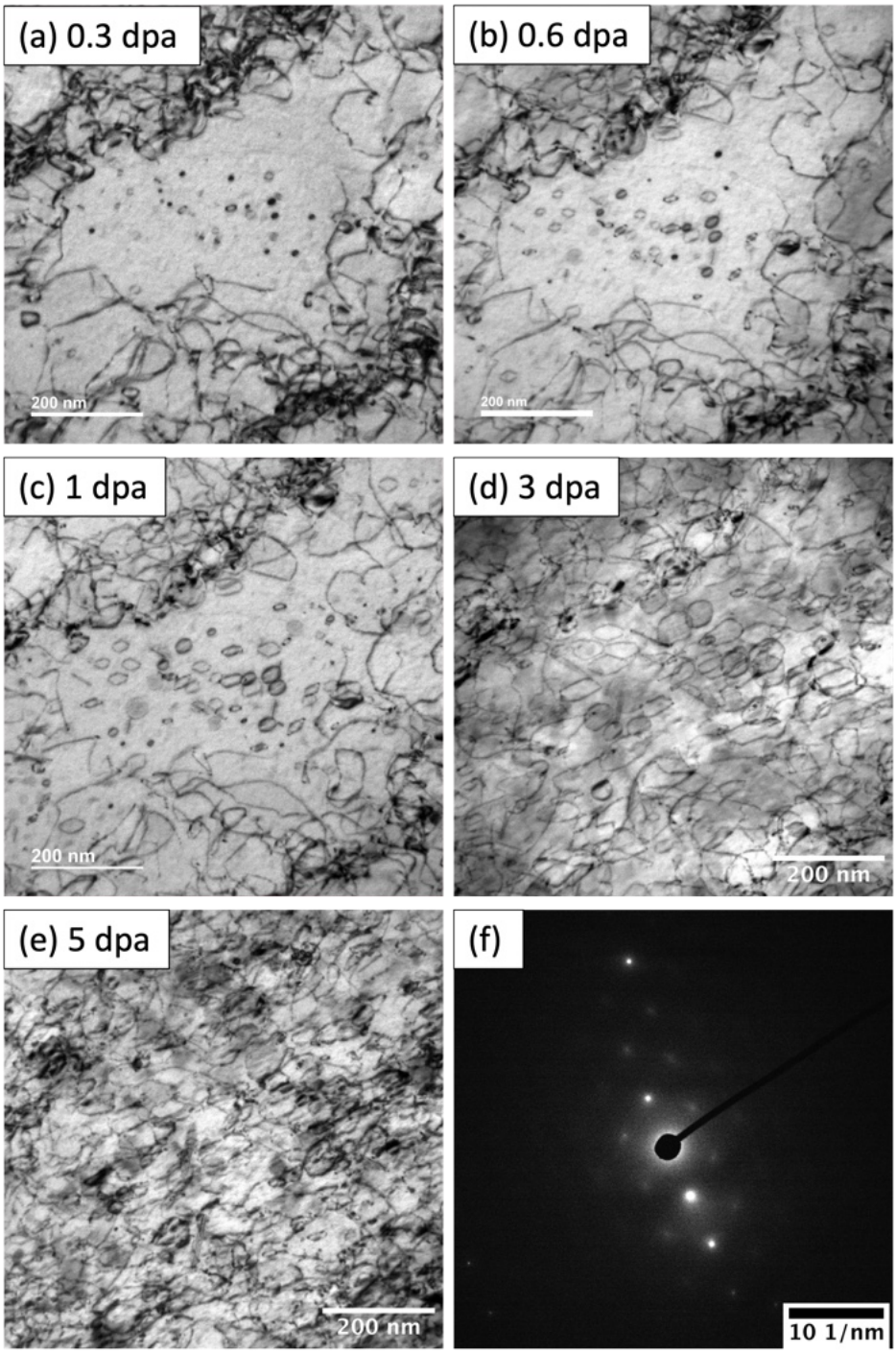

Figure 23. BF images showing the evolution of LPBF 316H *in-situ* irradiated with 1 MeV Kr^{2+} ions at 600°C to (a) 0.3 dpa, (b) 0.6 dpa, (c) 1 dpa, (d) 3 dpa and (e) 5 dpa. (f) the corresponding diffraction pattern indicating crystal orientation at 110 zone axis with g = 200 diffraction excited. The foil thickness estimated by EELS is 219 nm

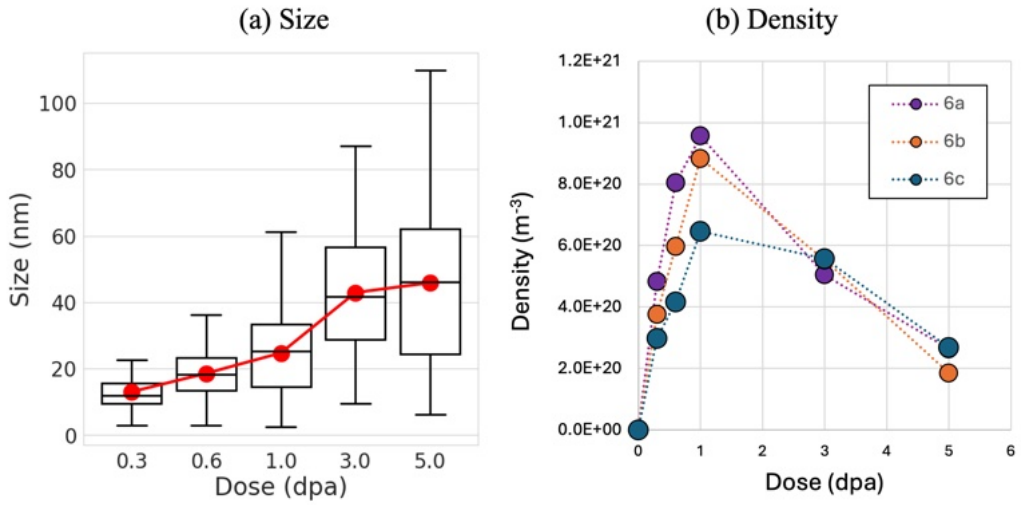

Figure 24. The (a) size and (b) density of dislocation loops observed in LPBF 316H *in-situ* irradiated with 1 MeV Kr^{2+} ions at 600°C. The measurements 6a, 6b and 6c correspond to areas specified in Supplemental Fig. S11.